Ages and fundamental properties of *Kepler* exoplanet host stars from asteroseismology

V. Silva Aguirre,[1]★ G. R. Davies,[1,2] S. Basu,[3] J. Christensen-Dalsgaard,[1]
O. Creevey,[4,5] T. S. Metcalfe,[1,6] T. R. Bedding,[1,7] L. Casagrande,[8] R. Handberg,[1,2]
M. N. Lund,[1,2] P. E. Nissen,[1] W. J. Chaplin,[1,2] D. Huber,[1,7,9] A. M. Serenelli,[10]
D. Stello,[1,7] V. Van Eylen,[1] T. L. Campante,[1,2] Y. Elsworth,[1,2] R. L. Gilliland,[11]
S. Hekker,[1,12] C. Karoff,[1,13] S. D. Kawaler,[14] H. Kjeldsen[1] and M. S. Lundkvist[1]

Affiliations are listed at the end of the paper

ABSTRACT

We present a study of 33 *Kepler* planet-candidate host stars for which asteroseismic observations have sufficiently high signal-to-noise ratio to allow extraction of individual pulsation frequencies. We implement a new Bayesian scheme that is flexible in its input to process individual oscillation frequencies, combinations of them, and average asteroseismic parameters, and derive robust fundamental properties for these targets. Applying this scheme to grids of evolutionary models yields stellar properties with median statistical uncertainties of 1.2 per cent (radius), 1.7 per cent (density), 3.3 per cent (mass), 4.4 per cent (distance), and 14 per cent (age), making this the exoplanet host-star sample with the most precise and uniformly determined fundamental parameters to date. We assess the systematics from changes in the solar abundances and mixing-length parameter, showing that they are smaller than the statistical errors. We also determine the stellar properties with three other fitting algorithms and explore the systematics arising from using different evolution and pulsation codes, resulting in 1 per cent in density and radius, and 2 per cent and 7 per cent in mass and age, respectively. We confirm previous findings of the initial helium abundance being a source of systematics comparable to our statistical uncertainties, and discuss future prospects for constraining this parameter by combining asteroseismology and data from space missions. Finally, we compare our derived properties with those obtained using the global average asteroseismic observables along with effective temperature and metallicity, finding excellent level of agreement. Owing to selection effects, our results show that the majority of the high signal-to-noise ratio asteroseismic *Kepler* host stars are older than the Sun.

Key words: asteroseismology – planets and satellites: fundamental parameters – stars: evolution – stars: fundamental parameters – stars: oscillations – planetary systems.

1 INTRODUCTION

The *CoRoT* and *Kepler* missions have revolutionized the quality and quantity of data that are available for the analysis of solar-like oscillations (see e.g. Chaplin & Miglio 2013). As a result, asteroseismology of solar-type stars has matured into a powerful tool to help characterize extrasolar planetary systems. Even a relatively straightforward analysis of solar-like oscillations can usually provide the surface gravity and mean density of an exoplanet host star with a

typical precision much higher than the constraints available from transit modelling (e.g. Huber et al. 2013b; Van Eylen & Albrecht 2015). With an independent effective temperature constraint, a precise stellar radius from asteroseismology can be obtained and used to determine the absolute planetary radius from transit photometry. The asteroseismic mass provides the absolute scale of the orbit, and when combined with transit-timing or radial velocity measurements yields the absolute planetary mass (Carter et al. 2012; Marcy et al. 2014). The asteroseismic age can be used to assess the dynamical stability of the system, and to establish its chronology with respect to other planetary systems. For the best and brightest targets, asteroseismology can also provide an independent determination of the

stellar rotation rate and inclination (Chaplin et al. 2013; Van Eylen et al. 2014; Davies et al. 2015). This can be used to probe spin–orbit alignment for systems without Rossiter–McLaughlin (R-M) measurements during transit, and it provides the full three-dimensional orientation when R-M measurements are available (e.g. Benomar et al. 2014; Lund et al. 2014). As a further matter, lower limits on the surface gravities of exoplanet host stars can still be placed in the event of a non-detection of solar-like oscillations (Campante et al. 2014).

Prior to the *CoRoT* and *Kepler* missions, solar-like oscillations were extremely difficult to observe for anything but the Sun, and data only existed for a handful of the brightest stars in the sky (e.g. Kjeldsen et al. 1995; Bouchy & Carrier 2001; Carrier, Eggenberger & Bouchy 2005; Arentoft et al. 2008). With the advent of space-born asteroseismic observations, thousands of detections have been possible for stars in different evolutionary stages (e.g. De Ridder et al. 2009; Huber et al. 2011). The focus of recent efforts has been to develop uniform data analysis and modelling strategies (Appourchaux et al. 2012; Chaplin et al. 2014), and to optimize the precision of asteroseismic inferences by matching the individual oscillation frequencies or ratios of characteristic frequency separations (Silva Aguirre et al. 2013; Metcalfe et al. 2014). These techniques typically improve the precision by a factor of 2 or more over methods that only use the global oscillation parameters (e.g. Mathur et al. 2012; Silva Aguirre et al. 2013; Lebreton & Goupil 2014), but the absolute accuracy is difficult to assess. Initial comparisons for the small samples of dwarfs and subgiants with well-determined distances and interferometric observations suggest consistency at the level of 4–5 per cent in stellar radii [Huber et al. 2012; Silva Aguirre et al. 2012, see also Miglio et al. (2013a) for a summary].

Future space-based photometry and astrometry, as well as complementary data from ground-based networks, will soon yield improved asteroseismic constraints for many exoplanet host stars. Observations of bright stars and clusters in the ecliptic plane have already started with *K2* (Howell et al. 2014), and the *TESS* mission will soon obtain similar data over the entire sky (Ricker et al. 2014). At the same time, the *Gaia* mission will determine improved parallaxes for all of these targets (Perryman et al. 2001), yielding luminosity constraints that could help break intrinsic parameter correlations in stellar models. The *PLATO* mission will build upon these successes with extended time series of many fields around the Galactic plane (Rauer et al. 2014), while ground-based spectroscopy from the Stellar Observations Network Group (SONG; Grundahl et al. 2008) will complement the satellite data for the brightest stars in the sky. Now is the time to address the underlying sources of systematic uncertainty in stellar properties determination, before this next deluge of observations. Exploration of biases in asteroseismic models and fitting methods for individual targets has been made (e.g. Miglio & Montalbán 2005; Lebreton & Goupil 2014), and we intend in this study to complement these efforts using a larger sample of stars together with a range of evolutionary and pulsation codes, and fitting algorithms.

In an accompanying paper (Davies et al., in preparation), the extraction of individual frequencies, combinations, and derivation of correlations has been performed for a sample of *Kepler* Objects of Interest (KOIs) with high-quality asteroseismic observations. We make use of these data to determine a robust set of fundamental properties, including ages, by introducing a new BAyesian STellar Algorithm (BASTA) and grids of evolutionary tracks specially constructed for this purpose. Our modelling strategy initially adopts this fitting algorithm and applies it to a fixed set of observables and modelling ingredients, and uses the results as the comparison basis

for quantifying the impact of additional input physics (e.g. diffusion, convective overshoot, mixing length, composition) in a systematic manner. We further explore the effects introduced by choosing different sets of asteroseismic observables, evolutionary and pulsation codes, as well as treatment of the pulsation data by determining stellar properties with three asteroseismic pipelines widely used in the literature.

This paper is organized as follows. In Section 2 we describe the target sample and define the observational quantities to be matched, while our new model grids and Bayesian analysis scheme are outlined in Section 3. The main results are discussed in Section 4, including a study of systematic uncertainties introduced by changes in the input physics and a thorough comparison with the results of asteroseismic fitting algorithms described in Appendix A. We use our derived stellar properties to check for consistency with the results from empirical scaling relations in Section 5, and explore possible correlations of planetary properties with age in Section 6. Conclusions and closing remarks are given in Section 7.

2 TARGET SELECTION AND DATA

Our sample has been extracted from the 77 exoplanet host stars presented in Huber et al. (2013b). These stars show clear signatures of stochastically excited oscillations with power spectra characterized by a Gaussian-shaped envelope centred on the frequency of maximum power $\nu_{\max}$. Pulsation modes of the same angular degree ℓ and consecutive radial order n are separated in frequency by a roughly constant spacing, known as the large frequency separation, defined as

$$\Delta \nu_\ell(n) = \nu_{n,\ell} - \nu_{n-1,\ell} . \tag{1}$$

Huber et al. (2013b) determined (for all 77 targets) the effective temperature T_{eff} and surface composition [Fe/H] from high-resolution spectroscopy, as well as the global average seismic parameters $\langle \Delta \nu \rangle$ and $\nu_{\max}$. From this sample, 35 stars have observations with high enough signal-to-noise ratios (SNRs) for reliable individual frequencies to be extracted (see the companion paper by Davies et al., in preparation). Typically, more than six consecutive modes are detected for each angular degree $\ell = 0$–2 allowing the construction of frequency combinations that aim at isolating the contribution of the inner structure from that of the outer layers. In particular, the frequency ratios r_{02}, r_{01}, and r_{10} defined as (Roxburgh & Vorontsov 2003)

$$r_{02}(n) = \frac{d_{02}(n)}{\Delta \nu_1(n)} \tag{2}$$

$$r_{01}(n) = \frac{d_{01}(n)}{\Delta \nu_1(n)}, \quad r_{10} = \frac{d_{10}(n)}{\Delta \nu_0(n+1)} , \tag{3}$$

where $d_{02}(n) = \nu_{n,0} - \nu_{n-1,2}$ is the small frequency separation and $d_{01}(n)$ and $d_{10}(n)$ are the smooth five-point small frequency separations:

$$d_{01}(n) = \frac{1}{8}(\nu_{n-1,0} - 4\nu_{n-1,1} + 6\nu_{n,0} - 4\nu_{n,1} + \nu_{n+1,0}) \tag{4}$$

$$d_{10}(n) = -\frac{1}{8}(\nu_{n-1,1} - 4\nu_{n,0} + 6\nu_{n,1} - 4\nu_{n+1,0} + \nu_{n+1,1}) . \tag{5}$$

The methods considered in this paper to determine stellar properties use different sets of asteroseismic observables in their optimization procedure (for details see Sections 3.2 and 4.3 below, as well as Appendix A): only the individual oscillation frequencies,

only the frequency ratios, or a weighted average of both sets. For reference, typical uncertainties in the three closest frequencies to ν_{max} are ~0.3 μHz (and below 0.1 μHz in the best cases), while fractional uncertainties in the same range for the frequency ratios are ~7 per cent (and smaller than 3 per cent in the highest SNR stars; further details can be found in the accompanying paper of Davies et al., in preparation). The advantage of using the ratios instead of the individual modes of oscillation is that they effectively suppress the contributions from the poorly modelled surface layers (see e.g. Otí Floranes, Christensen-Dalsgaard & Thompson 2005; Roxburgh 2005; Silva Aguirre et al. 2011a), and are insensitive to the line-of-sight Doppler velocity shift (Davies et al. 2014). This allows direct comparison of theoretical frequencies with the observed quantities without resorting to a *surface correction*, such as the power-law term applied to a solar model to reproduce the helioseismic observations (e.g. Kjeldsen, Bedding & Christensen-Dalsgaard 2008). Moreover, it has been shown that use of the frequency ratios provides the most precise results on asteroseismic ages as compared to fitting individual frequencies or using the scaling relations (Silva Aguirre et al. 2013; Lebreton & Goupil 2014).

The ratios and their corresponding covariance matrices have been obtained directly from the MCMC chains following the procedure described in Davies et al. (in preparation). It is customary to write the ratios $r_{01}(n)$ and $r_{10}(n)$ as one unique set of observables, called r_{010} (see Silva Aguirre et al. 2013):

$$r_{010} = \{r_{01}(n), r_{10}(n), r_{01}(n+1), r_{10}(n+1), \ldots\}. \quad (6)$$

While the frequency ratios provide a reliable proxy of the conditions in the deep stellar interior, their formulation is based on the assumption that the oscillation frequencies behave purely as pressure modes (Roxburgh & Vorontsov 2000, 2003, and references therein). Once a star exhausts its central hydrogen supply at the end of the main-sequence phase, its core contracts rapidly resulting in coupling between the propagation cavities of purely acoustic p modes and gravity g modes. Consequently, an oscillation mode can take mixed character and behave as a g mode in the central parts of the star while retaining its p-mode character in the outer layers; this feature is clearly visible in the échelle diagram (Grec, Fossat & Pomerantz 1983) as an *avoided crossing* (Aizenman, Smeyers & Weigert 1977).

The surface amplitudes of these mixed modes are smaller than those of pure p modes and they are therefore harder to detect. Of the 35 targets, 2 show clear evidence of modes with mixed character in their $\ell = 1$ frequencies, for which the ratios are not applicable. Their analysis will be presented elsewhere using tools especially designed for dealing with these types of oscillation modes (e.g. Deheuvels & Michel 2011; Benomar et al. 2012). A few of the remaining 33 stars show some hint of mixed modes starting to develop or seemingly present in their $\ell = 2$ ridges. In these cases, only the quantity r_{010} was matched as described in Section 3.2. Fig. 1 shows the échelle diagram of two KOIs from our sample. The mixed-mode nature in the $\ell = 2$ ridge around ~1070 μHz is very clear in the case of Kepler-36, while the ridge is completely smooth (and thus p-mode like) in the less evolved star Kepler-409.

The final sample of stars included in this study is shown in Fig. 2 together with theoretical stellar evolution tracks. Our targets span a wide range of effective temperatures ($5050 < T_{eff} < 6450$ K), metallicities ($-0.4 < $ [Fe/H] $ < +0.30$ dex), and evolutionary stages that will require the inclusion of different input physics to correctly determine their intrinsic properties.

3 STELLAR MODELS AND STATISTICAL ANALYSIS

The following sections describe the physical processes included in our stellar models, the Bayesian approach, assumptions and observables used to determine the central values and statistical uncertainties, and the adopted set of spectroscopic constraints of our targets. To test the effects in our derived stellar properties of different input physics, as well as properly accounting for systematic uncertainties in our results, we computed several grids of evolutionary tracks changing one physical ingredient at the time.

3.1 Grids of evolutionary models

We have computed grids of stellar models using the Garching Stellar Evolution Code (GARSTEC; Weiss & Schlattl 2008), summarized in Table 1. The basic input physics common to all grids includes the 2005 version of the OPAL equation of state (Rogers, Swenson & Iglesias 1996; Rogers & Nayfonov 2002), OPAL opacities for high temperatures (Iglesias & Rogers 1996) and those of Ferguson et al. (2005) for low temperatures, the NACRE compilation of nuclear reaction rates (Angulo et al. 1999) including the updated ^{14}N(p, γ)^{15}O reaction from Formicola et al. (2004), and the mixing-length theory of convection as described in Kippenhahn, Weigert & Weiss (2012).

In our computations, the quantity [Fe/H] is defined as [Fe/H] $= \log(Z_{sur}/X_{sur}) - \log(Z_{sur}/X_{sur})_{\odot}$, where Z_{sur} and X_{sur} correspond to the surface heavy-element and hydrogen fractions, respectively. This relation between [Fe/H] and Z/X is only valid if the element distribution relative to iron is the same in the observed star as in the Sun. A measurement of alpha abundances [α/Fe] is available from high-resolution spectroscopy for one of our targets (Kepler-444; see Campante et al. 2015). Their obtained average value of [α/Fe] $= +0.26 \pm 0.07$ has been transformed to Z/X using the prescription of Salaris, Chieffi & Straniero (1993).

The initial compositions of our evolutionary models were determined using a helium-to-metal enrichment law anchored to the big bang nucleosynthesis primordial values of $Z_0 = 0.0$ and $Y_0 = 0.248$ (Steigman 2010). A linear fit to the initial abundances of a solar calibration results in a relation close to $\Delta Y/\Delta Z = 1.4$, which is the one adopted in our grids (see e.g. Pietrinferni et al. 2004). The impact on stellar parameters of variations in the ratio between helium and heavy elements is explored in Section 4.4.

The efficiency of convection was determined from a standard solar calibration using microscopic diffusion (Thoul et al. 1994) and the Grevesse & Sauval (1998) solar mixture, resulting in $\alpha_{MLT} = 1.791$. Since GARSTEC does not include the effects of radiative levitation or turbulent mixing below the base of the convective envelope, we have restricted the calculations of the grid with diffusion to masses below 1.2 M$_{\odot}$ (see Turcotte, Richer & Michaud 1998). Our diffusion grid comprises masses between 0.7 and 1.2 M$_{\odot}$ in steps of 0.01 M$_{\odot}$ and initial compositions of $-0.65 < $ [Fe/H] $ < +0.50$ in steps of 0.05 dex. This mass range has been extended in our standard grid (i.e. without diffusion) to 0.7–1.8 M$_{\odot}$, also in steps of 0.01 M$_{\odot}$. Note that we have kept the value of α_{MLT} constant in these grids because solar models calibrated with and without diffusion show variations in this parameter of $\Delta\alpha_{MLT} \sim 0.12$ (see, e.g., Ciacio, Degl'innocenti & Ricci 1997). Our intention is to explore systematic uncertainties by changing one parameter at the time, and as part of this effort we explore larger changes in α_{MLT} (see below).

Furthermore, we constructed a grid including convective overshooting in the diffusive approach implemented in GARSTEC (see
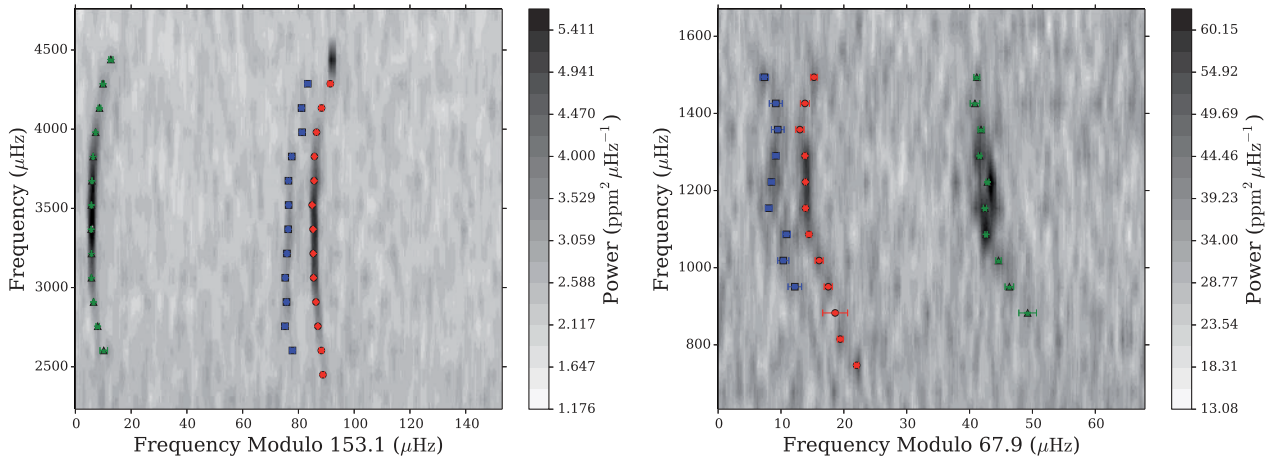
Figure 1. Échelle diagram of two selected targets from the sample. Symbols depict the different angular-degree values $\ell = 0$ (circles), $\ell = 1$ (triangles), and $\ell = 2$ (squares). Uncertainties in some frequencies are smaller than symbol sizes. Left: Kepler-409 shows the quasi-vertical alignment of its ridges as expected from pure p-mode frequencies. Right: Kepler-36 presents signature of modes with mixed character in the $\ell = 2$ ridge at ∼1070 μHz.
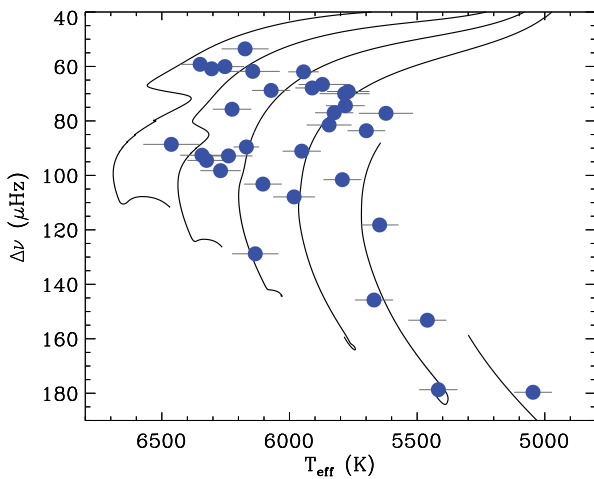

Figure 2. Sample distribution in the $T_{\rm eff}$ versus $\Delta\nu$ diagram, depicted over stellar evolutionary tracks at solar metallicity for masses between 0.8 and 1.3 M$_\odot$. Observational uncertainties in $\Delta\nu$ are smaller than the symbol size.

section 3.1.5 in Weiss & Schlattl 2008), using an efficiency of $\xi = 0.016$ that has been calibrated to open clusters (e.g. Magic et al. 2010; Silva Aguirre et al. 2011a) and is roughly equivalent to the $\alpha_{\rm ov} = 0.2$ pressure scaleheights commonly obtained when instantaneous mixing in the overshoot region is used. Additional grids of models were constructed changing the value of the mixing-

length parameter and the reference set of solar abundances (called GS98al+, GS98al−, and AS09 in Table 1, see also Section 4.2 below). The input physics of the grids is detailed in Table 1, and we will use the naming convention given there for the remainder of this paper.

For hundreds of models along each evolutionary track, we calculated theoretical oscillation frequencies using the Aarhus Adiabatic Oscillation Package (ADIPLS; Christensen-Dalsgaard 2008b). Each grid comprises over half a million models fully covering the spectroscopic and asteroseismic parameter space of our targets. The final stellar properties for our targets have been obtained with either the GS98dif or the GS98ove grids, for reasons thoroughly discussed in Sections 4.1.1 and 4.1.2 below.

3.2 Bayesian approach

The stellar properties of each star are determined using an adapted version of the Bayesian approach described in Serenelli et al. (2013) that we have named the BASTA. If $\boldsymbol{v}$ is a set of model stellar parameters (e.g. mass, composition, age), and $\mathcal{O}$ the observed data, then according to Bayes' rule the probability density function (PDF) of $\boldsymbol{v}$ given $\mathcal{O}$ is

$$p\left(\boldsymbol{v}|\mathcal{O}\right) \propto p\left(\boldsymbol{v}\right)\mathcal{L}\left(\mathcal{O}|\boldsymbol{v}\right). \tag{7}$$

Here, $\mathcal{L}\left(\mathcal{O}|\boldsymbol{v}\right)$ is the likelihood of $\mathcal{O}$ given $\boldsymbol{v}$ and $p\left(\boldsymbol{v}\right)$ is the prior PDF of $\boldsymbol{v}$ representing any prior knowledge on these quantities.

To determine $p\left(\boldsymbol{v}\right)$, we considered the following. The studied sample is comprised of stars presenting transit-like signals in their

Table 1. Description of the input physics considered in each of the grids of models. For all grids, mass separation is 0.01 M$_\odot$ and metallicity separation is 0.05 dex. When diffusion is included, this is done using the prescription of Thoul, Bahcall & Loeb (1994). Overshooting is incorporated as an exponential decay of the convective velocities (see Weiss & Schlattl 2008). Its efficiency has been calibrated with open clusters to $\xi = 0.016$ (Magic et al. 2010).

Name	Mass (M$_\odot$)	[Fe/H]	Solar abundances	Diffusion	Overshooting	$\alpha_{\rm MLT}$	$\Delta Y/\Delta Z$
GS98sta	0.70 ; 1.80	+0.50 ; −0.65	Grevesse & Sauval (1998)	No	No	1.791	1.4
GS98ove	1.00 ; 1.80	+0.50 ; −0.65	Grevesse & Sauval (1998)	No	Yes	1.791	1.4
GS98dif	0.70 ; 1.20	+0.50 ; −0.65	Grevesse & Sauval (1998)	Yes	No	1.791	1.4
GS98al+	0.70 ; 1.80	+0.50 ; −0.65	Grevesse & Sauval (1998)	No	No	2.091	1.4
GS98al−	0.70 ; 1.80	+0.50 ; −0.65	Grevesse & Sauval (1998)	No	No	1.491	1.4
AS09	0.70 ; 1.80	+0.50 ; −0.65	Asplund et al. (2009)	No	No	1.865	1.4

light curves, as well as stochastically excited oscillations. Since the selection function of pulsating exoplanet candidate host star observed by *Kepler* is complex, we cannot determine a prior probability for stellar properties based on these characteristics. Therefore, we assume a flat prior in [Fe/H] and age including only a strict cut on the latter at 15 Gyr (to properly construct the age PDF of old stars), and we use a standard Salpeter initial mass function.

We compute the likelihood of the observed values $\mathcal{O}$ given a set of model parameters $\boldsymbol{v}$ assuming Gaussian distributed errors. BASTA is flexible in its input, and the observables included can be the spectroscopic parameters ($T_{\rm eff}$, [Fe/H], log g), the individual oscillation frequencies, the global average asteroseismic parameters $\langle \Delta \nu \rangle$ and $\nu_{\rm max}$, the frequency ratios r_{02} and r_{010} defined in equations (2) and (6), or any combination of the aforementioned quantities. The construction of the ratios introduces correlations as a function of frequency which are taken into account in the likelihood calculation of each model:

$$\mathcal{L}(\mathcal{O}|\boldsymbol{v}) = \frac{1}{(2\pi)^{1/2}\sqrt{|\mathbf{C}|}} \exp\left(-\chi^2/2\right) \tag{8}$$

$$\chi^2 = (\boldsymbol{o}_{\rm obs} - \boldsymbol{o}_{\rm model})^{\rm T}\, \mathbf{C}^{-1}\, (\boldsymbol{o}_{\rm obs} - \boldsymbol{o}_{\rm model})\,, \tag{9}$$

where $\mathbf{C}$ is the covariance matrix of the observed values $\boldsymbol{o}_{\rm obs}$ and $\boldsymbol{o}_{\rm model}$ are the same quantities determined from the model. For computational efficiency, we preselect models for determining the likelihood within 500 K and 0.5 dex of the spectroscopic $T_{\rm eff}$ and [Fe/H] values, and having an average large frequency separation $\langle \Delta \nu \rangle$ within 15 per cent of the observed one (approximately 3σ from the median uncertainty for the majority of the asteroseismic *Kepler* solar-type sample; see Chaplin et al. 2014). The value of $\langle \Delta \nu \rangle$ in the models is obtained using theoretical frequencies of oscillation following the prescription of White et al. (2011, see Section 5 below).

Our final values for stellar properties of all targets were determined with BASTA and GARSTEC grids using $T_{\rm eff}$, [Fe/H], and the frequency ratios r_{010} and r_{02} as the observables included in the likelihood calculation (except in a few cases where only r_{010} was fitted because $\ell = 2$ mixed modes prevented us from using r_{02}, see Section 2). For comparison, we have also determined all stellar properties using the individual oscillation frequencies (see Section 4.3) and the global average parameters $\langle \Delta \nu \rangle$ and $\nu_{\rm max}$ (see Section 5) as the asteroseismic data to be fitted.

Recently, Roxburgh & Vorontsov (2013) proposed that fitting the separation ratios r_{010} and r_{02} as a function of radial order could lead to biases in the determined stellar structure, and recommended comparing observations with models by interpolating the theoretical ratios at the observed central frequencies. We have implemented this fit in BASTA and found no significant difference with the results obtained when comparing at a fixed radial order. Similar conclusions were given by Lebreton & Goupil (2014, see their appendix A.1).

Once the PDF has been computed using the definitions above, the marginalized posterior PDF of any stellar quantity x is obtained as

$$p(x|\mathcal{O}) = \int \delta(x(\boldsymbol{v}) - x) p(\boldsymbol{v}|\mathcal{O}) w_v \mathrm{d}^3 v, \tag{10}$$

where w_v are the appropriate weights used to account for the volume of parameter space occupied by a stellar track point characterized by $\boldsymbol{v}$, i.e. half the distance to its neighbouring points in mass, metallicity, and age. The final values reported for each stellar quantity are obtained from the median of the posterior PDF and the 16 and 84 percentiles.

3.3 Spectroscopic input parameters

We initially adopted the spectroscopic values reported in Huber et al. (2013b) as input parameters in the Bayesian procedure described above. Since this approach allows determination of the posterior PDF from models of any stellar quantity, a comparison showed that in two stars the best asteroseismic solutions favoured atmospheric parameters not compatible with the spectroscopic ones. To explore the reasons for this discrepancy, we have made a new determination of $T_{\rm eff}$ and [Fe/H] from high-resolution spectra on these single targets as available on the website of the Kepler Community Follow-up Observing Program (CFOP[1]).

The method takes advantage of the accurate values of the stellar surface gravity, log g, determined from seismic data, which allows a determination of $T_{\rm eff}$ from the requirement that the Fe I and Fe II lines should give the same Fe abundance. Given that [Fe/H] derived from Fe I lines *increases* by ~0.055 dex for solar-type stars when $T_{\rm eff}$ is increased by 100 K, and that [Fe/H] based on Fe II lines *decreases* by ~0.03 dex for the same change in $T_{\rm eff}$, the method leads to precise values of $T_{\rm eff}$ (± 70 K) if the two [Fe/H] values are determined with errors less than ± 0.03 dex.

This is possible when high-resolution spectra having SNR > 40 are analysed differentially with respect to the Sun. Based on the solar spectrum we have selected 39 Fe I and 14 Fe II unblended lines in the wavelength region 480–650 nm. Their equivalent widths (EWs), which range from 30 to 80 mÅ in the stellar spectra, were measured by Gaussian fitting to the line profiles and analysed with MARCS model atmospheres (Gustafsson et al. 2008) to provide local thermodynamic equilibrium (LTE) abundances as described in Nissen et al. (2014). The Fe abundances from Fe I lines are subject to small non-LTE effects, which were taken into account using the calculations of Lind, Bergemann & Asplund (2012). These corrections decrease the derived $T_{\rm eff}$ by 15–30 K.

The abundances are based on medium to strong spectral lines that are sensitive to the microturbulence velocity $\xi_{\rm turb}$. This parameter is not well constrained from the set of lines used, and we have therefore adopted a relation $\xi_{\rm turb}$ (km s^{-1})=1.0 + 0.000 63($T_{\rm eff}$ − 5777) − 0.54(log g − 4.44) derived for solar-type stars with high-SNR HARPS spectra (Nissen et al. 2014). The derived $T_{\rm eff}$ is not very sensitive to $\xi_{\rm turb}$, because the two sets of Fe I and Fe II lines have about the same average EW. For an estimated error of 0.2 km s^{-1} in $\xi_{\rm turb}$, the error in $T_{\rm eff}$ is 25 K, whereas the corresponding error in the derived [Fe/H] is 0.05 dex. Furthermore, we note that an error of 0.05 dex in log g induces an error of 20 K in $T_{\rm eff}$, and has a negligible effect (<0.01 dex) on [Fe/H].

The results obtained are given in Table 2. The listed errors correspond to the uncertainties in [Fe/H] estimated from the line-to-line scatter of the derived abundances. The small errors arising from the uncertainties in log g and $\xi_{\rm turb}$ were added in quadrature. For the two stars in Table 2, $T_{\rm eff}$ and [Fe/H] deviate significantly from the values determined in previous studies, i.e. KOI-5 ($T_{\rm eff} = 5753 \pm 75$ K, [Fe/H] = 0.05 ± 0.1 dex; Huber et al. 2013b) and Kepler-21 ($T_{\rm eff} = 6131 \pm 44$ K, [Fe/H] = -0.15 ± 0.06 dex; Howell et al. 2012). The final stellar properties in this paper were determined using these updated results. We emphasize that, for completeness, we analysed another five stars from the Huber et al. (2013b) sample and found good agreement: average differences and standard deviations for these targets [new

---

[1] https://cfop.ipac.caltech.edu/home/

Table 2. Spectroscopic determinations of selected KOIs. The log g values were adopted from asteroseismic determinations of Huber et al. (2013b). Uncertainties quoted in $T_{\rm eff}$ and [Fe/H] correspond to the internal precision of the method.

Name	Spectrum	SNR	$T_{\rm eff}$ (K)	log g (dex)	[Fe/H] (dex)	$\xi_{\rm turb}$ (km s^{-1})
KOI-5	McD2.7m	70	5945 ± 60	4.05	$+0.17 \pm 0.05$	1.3
Kepler-21	TRES	150	6305 ± 50	4.02	-0.03 ± 0.05	1.6

values – Huber et al. (2013b) values] are $\Delta T_{\rm eff} = -13 \pm 70$ K and $\Delta[{\rm Fe/H}] = -0.06 \pm 0.06$ dex.

4 RESULTS

To determine the final stellar properties and uncertainties of our sample, we have devised the following procedure. The central values and statistical uncertainties were obtained using the BASTA and a choice of GARSTEC grids including different input physics as described in Section 4.1. These are the recommended stellar properties of the sample and are listed in Table 3. We then explored the impact of changing the reference solar abundances and mixing-length parameter (Section 4.2) to estimate a systematic uncertainty from the input physics. We then compared our results with those obtained from three different asteroseismic pipelines, providing a systematic uncertainty arising from the use of different evolution codes and fitting algorithms (Section 4.3). Finally, we estimated a systematic uncertainty arising from our choice of $\Delta Y/\Delta Z = 1.4$ (Section 4.4), and discuss the possibility of breaking the degeneracy between helium and mass using *Gaia* results.

4.1 Adopted physics for stellar properties and statistical uncertainties

The BASTA described in Section 3.2 was initially applied to the sample using the standard grid (GS98sta, see Table 1). Fig. 3 shows the obtained distribution of masses for the targets, encompassing a range between ∼0.75 and 1.6 M$_\odot$. There are several physical processes that can considerably affect the main-sequence evolution of stars, but whose efficiency and range of applicability are not fully constrained by theory or independent observations. We explore in the following sections the cases of microscopic diffusion and overshooting.

4.1.1 Microscopic diffusion

In the low-mass regime, neglecting the effects of microscopic diffusion can have significant impact on the determined properties. If stars are indeed subject to element settling throughout their main-sequence lifetimes, the derived ages can be particularly biased (e.g. Valle et al. 2014). Evidence for the occurrence of microscopic diffusion is clear for the Sun (e.g. Christensen-Dalsgaard, Proffitt & Thompson 1993; Guzik & Cox 1993) and has been growing in recent years for star clusters (see e.g. Korn et al. 2007; Gruyters et al. 2013; Önehag, Gustafsson & Korn 2014) revealing the importance of this process in low-mass stars.

Using the grid of models that includes the effects of diffusion (GS98dif), we have redetermined the stellar properties of all stars with masses predicted from the standard grid to be below ∼1.2 M$_\odot$. The top panel of Fig. 4 shows the resulting fractional mass differences, with the two determinations typically agreeing within ∼2.5 per cent. There is no visible trend as a function of metallicity although the largest differences are found for the most metal-poor

stars, as expected (see e.g. Valle et al. 2014). However, the ages predicted by the standard grid are systematically older than those based on diffusion (bottom panel in Fig. 4). Since the masses determined from both grids agree on average, this behaviour is not what would be expected from a pure mass effect and is a consequence of several physical effects combined that balance each other.

Stellar models that include microscopic diffusion sink helium and heavy elements while diffusing hydrogen towards the surface during their main-sequence lifetime. This process effectively reduces the amount of fuel available in the core producing a faster main-sequence evolution and therefore decreasing the age a model has at a given mean density. Interestingly, the effects of diffusion on age counterbalance those expected from a pure mass effect, since even if the mass predicted by the non-diffusive model is higher than the diffusive one, its age remains older. Thus, despite not producing biases in the masses determined, the use of diffusion does affect the ages obtained from asteroseismic fitting and should be taken into account in the relevant regime. Similar results were found by e.g. Miglio & Montalbán (2005) and Valle et al. (2015), where models with diffusion predict younger ages than those not including this effect.

Compared to canonical models, the transport of chemical species by microscopic diffusion produces different composition profiles and therefore different opacity values through the stellar interior. As a consequence, evolutionary tracks computed with the same initial chemical mixture including or not these effects will also show a different effective temperature evolution during the main-sequence phase. An example of the effects played by microscopic diffusion is shown in Fig. 5. These results are obtained for Kepler-93 using the frequency ratios r_{010}, r_{02}, and spectroscopic parameters as the observational data to be reproduced. The plots depict the χ^2 surface from each grid of models in the $T_{\rm eff}$ versus [Fe/H] plane as well as the observed spectroscopic properties and uncertainties. Due to the number of observables and size of the fractional uncertainties, the fit is dominated by the asteroseismic data and the grid neglecting diffusion favours a parameter space that is not fully compatible with the observed $T_{\rm eff}$ and [Fe/H] of the target. In particular, GS98sta results predict $T_{\rm eff}$ values too high compared with the spectroscopic ones. For this reason, the grid with diffusion has been used for determining the final central values and statistical uncertainties of targets with masses below ∼1.2 M$_\odot$.

One must be cautious when determining uncertainties using the diffusion grid because it suffers from an unavoidable edge effect for masses above ∼1.15 M$_\odot$, where the posterior PDF are artificially cut due to the chosen upper mass limit when constructing the grid (1.20 M$_\odot$). To ensure a smooth transition in the obtained stellar properties when switching from GS98dif to another grid, we compared the results predicted with GS98sta and GS98ove to those of GS98dif in six targets at the edge of this mass range (KOI-5, Kepler-65, Kepler-25, Kepler-126, KOI-268, and Kepler-129; see Table 3). All stars where the GS98dif grid returned central mass values above 1.15 M$_\odot$ clearly showed the edge effect in the uncertainties, but the central values in the stellar properties are fully

Table 3. The full table is available in electronic format on the journal website. Recommended set of stellar properties and statistical uncertainties of exoplanet candidate host stars as determined with BASTA. Solar luminosity used $L_\odot = 3.846 \times 10^{33}$ (erg s^{-1}). Additional systematic uncertainties can be accounted for (see Sections 4.2, 4.3, and 4.4): from input physics of 0.8 per cent (density), 0.7 per cent (radius), 2.3 per cent (mass), 9.6 per cent (age); from choice of observables of 0.3 per cent (density and radius), 1 per cent (mass), and 7 per cent (age); from fitting algorithms and codes of 1 per cent (density and radius), 2 per cent (mass), and 9 per cent (age); from the initial helium abundance of 1.7 per cent (density), 1.6 per cent (radius), 3.6 per cent (mass), and 16.8 per cent (age). Reference column gives literature sources of confirmed or validated exoplanets.

KOI	KIC	T_{eff} (K)	[Fe/H] (dex)	Mass ($M_\odot$)	Radius ($R_\odot$)	Density (g cm^{-3})	BASTA log g (dex)	Luminosity ($L_\odot$)	Age (Gyr)	Distance (pc)	Notes	Reference
2	10666592	6350 ± 80	0.26 ± 0.08	$1.497^{+0.042}_{-0.040}$	$1.986^{+0.018}_{-0.015}$	$0.269^{+0.004}_{-0.005}$	$4.017^{+0.007}_{-0.009}$	$5.754^{+0.304}_{-0.322}$	$2.11^{+0.29}_{-0.24}$	$386.44^{+12.11}_{-11.95}$	HAT-P7	Pál et al. (2008)
5	8554498	5945 ± 60	0.17 ± 0.05	$1.197^{+0.021}_{-0.029}$	$1.794^{+0.015}_{-0.015}$	$0.292^{+0.003}_{-0.003}$	$4.007^{+0.003}_{-0.003}$	$3.684^{+0.130}_{-0.182}$	$5.60^{+0.45}_{-0.42}$	$439.34^{+13.68}_{-13.68}$		
7	11853905	5781 ± 76	0.09 ± 0.10	$1.117^{+0.021}_{-0.029}$	$1.555^{+0.012}_{-0.012}$	$0.419^{+0.004}_{-0.006}$	$4.102^{+0.005}_{-0.004}$	$2.505^{+0.142}_{-0.124}$	$6.71^{+0.77}_{-0.67}$	$499.10^{+15.46}_{-15.46}$	Kepler-4	Borucki et al. (2010)
41	6521045	5825 ± 75	0.02 ± 0.10	$1.108^{+0.021}_{-0.019}$	$1.513^{+0.009}_{-0.012}$	$0.454^{+0.004}_{-0.006}$	$4.125^{+0.004}_{-0.004}$	$2.478^{+0.112}_{-0.112}$	$6.50^{+0.46}_{-0.56}$	$310.34^{+9.49}_{-9.63}$	Kepler-100	Marcy et al. (2014)
42	8866102	6325 ± 75	0.01 ± 0.10	$1.228^{+0.042}_{-0.040}$	$1.357^{+0.012}_{-0.015}$	$0.695^{+0.010}_{-0.011}$	$4.262^{+0.007}_{-0.008}$	$2.753^{+0.130}_{-0.130}$	$2.60^{+0.56}_{-0.53}$	$140.83^{+4.40}_{-4.50}$	Kepler-410 A	Van Eylen et al. (2014)
69	3544595	5669 ± 75	-0.18 ± 0.10	$0.899^{+0.009}_{-0.009}$	$0.916^{+0.006}_{-0.006}$	$1.653^{+0.016}_{-0.018}$	$4.468^{+0.003}_{-0.003}$	$0.780^{+0.029}_{-0.025}$	$6.63^{+0.62}_{-0.57}$	$92.77^{+2.85}_{-2.85}$	Kepler-93	Ballard et al. (2014)
72	11904151	5647 ± 74	-0.15 ± 0.10	$0.918^{+0.011}_{-0.019}$	$1.066^{+0.006}_{-0.009}$	$1.068^{+0.007}_{-0.012}$	$4.344^{+0.003}_{-0.003}$	$1.063^{+0.032}_{-0.034}$	$10.23^{+0.83}_{-0.67}$	$179.01^{+5.46}_{-5.58}$	Kepler-10	Batalha et al. (2011)^a
85	5866724	6169 ± 50	0.09 ± 0.08	$1.199^{+0.029}_{-0.030}$	$1.399^{+0.012}_{-0.012}$	$0.616^{+0.007}_{-0.008}$	$4.224^{+0.005}_{-0.007}$	$2.577^{+0.103}_{-0.095}$	$3.89^{+0.59}_{-0.48}$	$312.43^{+9.75}_{-9.75}$	Kepler-65	Chaplin et al. (2013)
108	4914423	5845 ± 88	0.07 ± 0.11	$1.099^{+0.019}_{-0.030}$	$1.450^{+0.009}_{-0.009}$	$0.507^{+0.005}_{-0.005}$	$4.155^{+0.004}_{-0.004}$	$2.256^{+0.115}_{-0.119}$	$6.67^{+0.69}_{-0.62}$	$473.56^{+14.51}_{-14.51}$	Kepler-103	Marcy et al. (2014)
122	8349582	5699 ± 74	0.30 ± 0.10	$1.068^{+0.021}_{-0.019}$	$1.417^{+0.012}_{-0.009}$	$0.528^{+0.006}_{-0.005}$	$4.163^{+0.003}_{-0.004}$	$1.891^{+0.090}_{-0.094}$	$8.03^{+0.80}_{-0.70}$	$413.66^{+12.89}_{-12.89}$	Kepler-95	Marcy et al. (2014)
123	5094751	5952 ± 75	-0.08 ± 0.10	$1.068^{+0.040}_{-0.040}$	$1.339^{+0.015}_{-0.018}$	$0.628^{+0.008}_{-0.007}$	$4.213^{+0.008}_{-0.007}$	$2.040^{+0.124}_{-0.112}$	$6.35^{+1.05}_{-1.05}$	$464.73^{+14.88}_{-15.28}$	Kepler-109	Marcy et al. (2014)
244	4349452	6270 ± 79	-0.04 ± 0.10	$1.159^{+0.040}_{-0.051}$	$1.297^{+0.015}_{-0.015}$	$0.745^{+0.009}_{-0.010}$	$4.275^{+0.007}_{-0.008}$	$2.406^{+0.126}_{-0.128}$	$3.45^{+0.81}_{-0.72}$	$247.49^{+7.96}_{-7.96}$	Kepler-25	Steffen et al. (2012)
245	8478994	5417 ± 75	-0.32 ± 0.07	$0.810^{+0.019}_{-0.011}$	$0.772^{+0.003}_{-0.006}$	$2.486^{+0.022}_{-0.025}$	$4.570^{+0.003}_{-0.002}$	$0.467^{+0.023}_{-0.025}$	$5.35^{+0.91}_{-1.01}$	$63.96^{+1.93}_{-1.98}$	Kepler-37	Barclay et al. (2013)
246	11295426	5793 ± 74	0.12 ± 0.07	$1.068^{+0.011}_{-0.019}$	$1.237^{+0.006}_{-0.006}$	$0.795^{+0.005}_{-0.011}$	$4.280^{+0.003}_{-0.003}$	$1.581^{+0.043}_{-0.040}$	$6.31^{+0.32}_{-0.34}$	$139.77^{+4.25}_{-4.25}$	Kepler-68	Gilliland et al. (2013)
260	8292840	6239 ± 94	-0.14 ± 0.10	$1.148^{+0.051}_{-0.049}$	$1.345^{+0.015}_{-0.018}$	$0.666^{+0.010}_{-0.010}$	$4.240^{+0.008}_{-0.008}$	$2.636^{+0.148}_{-0.142}$	$3.85^{+0.81}_{-0.75}$	$240.28^{+7.69}_{-7.89}$	Kepler-126	Rowe et al. (2014)
262	11807274	6225 ± 75	-0.00 ± 0.08	$1.239^{+0.040}_{-0.040}$	$1.582^{+0.015}_{-0.021}$	$0.444^{+0.007}_{-0.007}$	$4.135^{+0.007}_{-0.009}$	$3.466^{+0.167}_{-0.157}$	$3.59^{+0.78}_{-0.45}$	$251.15^{+7.90}_{-8.24}$	Kepler-50	Steffen et al. (2013)
263	10514430	5784 ± 98	-0.11 ± 0.11	$1.059^{+0.040}_{-0.021}$	$1.590^{+0.015}_{-0.018}$	$0.374^{+0.004}_{-0.004}$	$4.061^{+0.004}_{-0.004}$	$2.634^{+0.151}_{-0.124}$	$7.84^{+0.40}_{-0.91}$	$211.53^{+6.65}_{-6.78}$	False-positive^b	
268	3425851	6343 ± 85	-0.04 ± 0.10	$1.178^{+0.049}_{-0.021}$	$1.360^{+0.015}_{-0.018}$	$0.662^{+0.009}_{-0.008}$	$4.243^{+0.008}_{-0.008}$	$2.728^{+0.162}_{-0.157}$	$3.32^{+0.85}_{-0.64}$	$244.81^{+7.82}_{-8.03}$		
269	7670943	6463 ± 110	0.09 ± 0.11	$1.239^{+0.040}_{-0.051}$	$1.417^{+0.015}_{-0.021}$	$0.616^{+0.009}_{-0.010}$	$4.228^{+0.008}_{-0.008}$	$3.039^{+0.167}_{-0.173}$	$2.78^{+0.62}_{-0.51}$	$331.99^{+10.56}_{-11.11}$		
274	8077137	6072 ± 75	-0.09 ± 0.10	$1.117^{+0.040}_{-0.049}$	$1.632^{+0.018}_{-0.009}$	$0.361^{+0.006}_{-0.006}$	$4.056^{+0.013}_{-0.010}$	$3.183^{+0.293}_{-0.202}$	$6.23^{+0.56}_{-1.23}$	$413.44^{+13.21}_{-12.61}$	Kepler-128	Xie (2014)
275	10586004	5770 ± 83	0.29 ± 0.10	$1.178^{+0.021}_{-0.030}$	$1.653^{+0.009}_{-0.012}$	$0.367^{+0.004}_{-0.005}$	$4.071^{+0.005}_{-0.005}$	$2.749^{+0.151}_{-0.155}$	$6.43^{+0.64}_{-0.61}$	$402.73^{+12.28}_{-12.43}$	Kepler-129	Rowe et al. (2014)
276	11133306	5982 ± 82	-0.02 ± 0.10	$1.059^{+0.040}_{-0.030}$	$1.189^{+0.012}_{-0.012}$	$0.891^{+0.008}_{-0.009}$	$4.314^{+0.004}_{-0.007}$	$1.628^{+0.092}_{-0.079}$	$5.14^{+0.86}_{-0.88}$	$331.57^{+10.50}_{-10.50}$		
277	11401755	5911 ± 66	-0.20 ± 0.06	$1.059^{+0.030}_{-0.021}$	$1.632^{+0.015}_{-0.021}$	$0.346^{+0.003}_{-0.006}$	$4.039^{+0.004}_{-0.004}$	$2.982^{+0.144}_{-0.148}$	$7.10^{+0.61}_{-0.59}$	$514.89^{+16.15}_{-16.81}$	Kepler-36	Carter et al. (2012)
280	4141376	6134 ± 91	-0.24 ± 0.10	$1.019^{+0.021}_{-0.030}$	$1.039^{+0.009}_{-0.009}$	$1.278^{+0.011}_{-0.013}$	$4.412^{+0.003}_{-0.004}$	$1.363^{+0.052}_{-0.056}$	$3.27^{+0.59}_{-0.64}$	$222.15^{+6.94}_{-6.94}$		
281	4143755	5622 ± 106	-0.40 ± 0.11	$0.918^{+0.021}_{-0.030}$	$1.414^{+0.012}_{-0.013}$	$0.456^{+0.006}_{-0.006}$	$4.102^{+0.001}_{-0.002}$	$1.997^{+0.029}_{-0.038}$	$11.27^{+1.50}_{-1.35}$	$360.19^{+11.23}_{-11.30}$		
285	6196457	5871 ± 94	0.17 ± 0.11	$1.209^{+0.019}_{-0.030}$	$1.716^{+0.012}_{-0.012}$	$0.335^{+0.004}_{-0.004}$	$4.049^{+0.004}_{-0.005}$	$3.316^{+0.185}_{-0.164}$	$5.52^{+0.51}_{-0.48}$	$448.57^{+13.82}_{-13.82}$	Kepler-92	Xie (2014)
288	9592705	6174 ± 92	0.22 ± 0.10	$1.509^{+0.029}_{-0.021}$	$2.124^{+0.015}_{-0.012}$	$0.221^{+0.003}_{-0.003}$	$3.961^{+0.004}_{-0.003}$	$6.088^{+0.227}_{-0.247}$	$2.33^{+0.18}_{-0.16}$	$428.89^{+13.22}_{-13.09}$		
370	8494142	6144 ± 106	0.13 ± 0.10	$1.418^{+0.030}_{-0.021}$	$1.887^{+0.012}_{-0.012}$	$0.298^{+0.005}_{-0.005}$	$4.038^{+0.005}_{-0.005}$	$4.818^{+0.259}_{-0.243}$	$2.62^{+0.26}_{-0.24}$	$584.10^{+17.91}_{-17.91}$	Kepler-145	Xie (2014)
974	9414417	6253 ± 75	-0.13 ± 0.10	$1.387^{+0.021}_{-0.009}$	$1.914^{+0.015}_{-0.015}$	$0.280^{+0.004}_{-0.005}$	$4.017^{+0.004}_{-0.004}$	$5.343^{+0.157}_{-0.157}$	$2.65^{+0.14}_{-0.16}$	$232.81^{+7.22}_{-7.22}$		
975	3632418	6305 ± 50	-0.03 ± 0.10	$1.408^{+0.021}_{-0.030}$	$1.902^{+0.018}_{-0.012}$	$0.287^{+0.004}_{-0.005}$	$4.026^{+0.004}_{-0.004}$	$5.188^{+0.142}_{-0.128}$	$2.60^{+0.16}_{-0.16}$	$114.49^{+3.60}_{-7.22}$	Kepler-21	Howell et al. (2012)
1612	10963065	6104 ± 74	-0.20 ± 0.10	$1.089^{+0.019}_{-0.030}$	$1.228^{+0.012}_{-0.009}$	$0.823^{+0.010}_{-0.009}$	$4.293^{+0.004}_{-0.004}$	$1.961^{+0.058}_{-0.058}$	$4.18^{+0.53}_{-0.35}$	$92.37^{+2.91}_{-2.85}$	Kepler-408	Marcy et al. (2014)
1925	9955598	5460 ± 75	0.08 ± 0.10	$0.890^{+0.009}_{-0.011}$	$0.883^{+0.003}_{-0.006}$	$1.821^{+0.018}_{-0.018}$	$4.495^{+0.002}_{-0.002}$	$0.598^{+0.025}_{-0.023}$	$6.98^{+0.40}_{-0.50}$	$66.80^{+2.02}_{-2.05}$	Kepler-409	Marcy et al. (2014)
3158	6278762	5046 ± 74	-0.37 ± 0.09	$0.739^{+0.009}_{-0.011}$	$0.748^{+0.006}_{-0.003}$	$2.498^{+0.018}_{-0.025}$	$4.560^{+0.003}_{-0.002}$	$0.341^{+0.020}_{-0.016}$	$11.54^{+0.99}_{-0.94}$	$32.90^{+1.02}_{-1.00}$	Kepler-444	Campante et al. (2015)

^{a}See also Fressin et al. (2011). ^{b}Ephemeris match indicates contamination, see CFOP website (https://cfop.ipac.caltech.edu/home/).
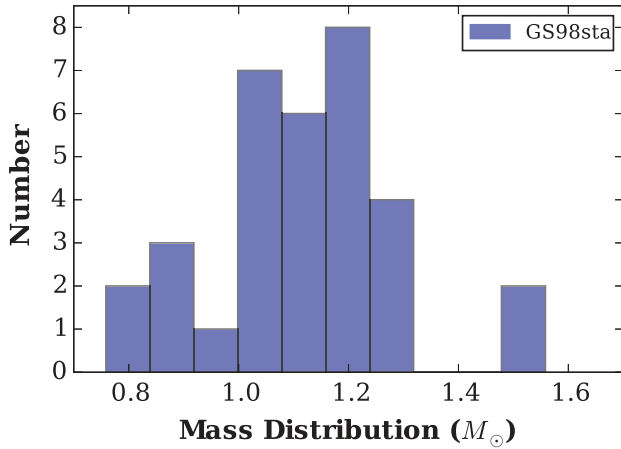
Figure 3. Mass distribution of the sample obtained using the standard grid (GS98sta).

compatible with those obtained from the other two grids (note that the effects of overshooting are not expected to be significant in the 1.15–1.2 $M_\odot$ range; see Section 4.1.2 below). The reason is that for these masses, the evolutionary time-scale is short enough for the effects of diffusion to be minor. Thus, in our recommended values presented in Table 3, we restrict ourselves to the diffusion grid in all stars with central mass values below 1.15 $M_\odot$.

4.1.2 Convective overshooting

In stars with masses higher than ~1.1 $M_\odot$, the size of the convective core severely affects the age at which central hydrogen exhaustion (the terminal-age main-sequence, TAMS) is reached. The extent of the central mixed region is controlled by the convective overshoot efficiency, a free parameter in stellar evolution calculations. There is a wealth of evidence in the literature that convective core sizes are probably larger than those predicted by models applying the pure Schwarzschild criterion for convective boundary determination (e.g. Maeder 1974a,b; Maeder & Meynet 1991; Chiosi, Bertelli & Bressan 1992; Vandenberg et al. 2007, just to name a few), and recent analyses of *Kepler* stars have further supported this scenario (Silva Aguirre et al. 2013). Thus, we have applied our Bayesian
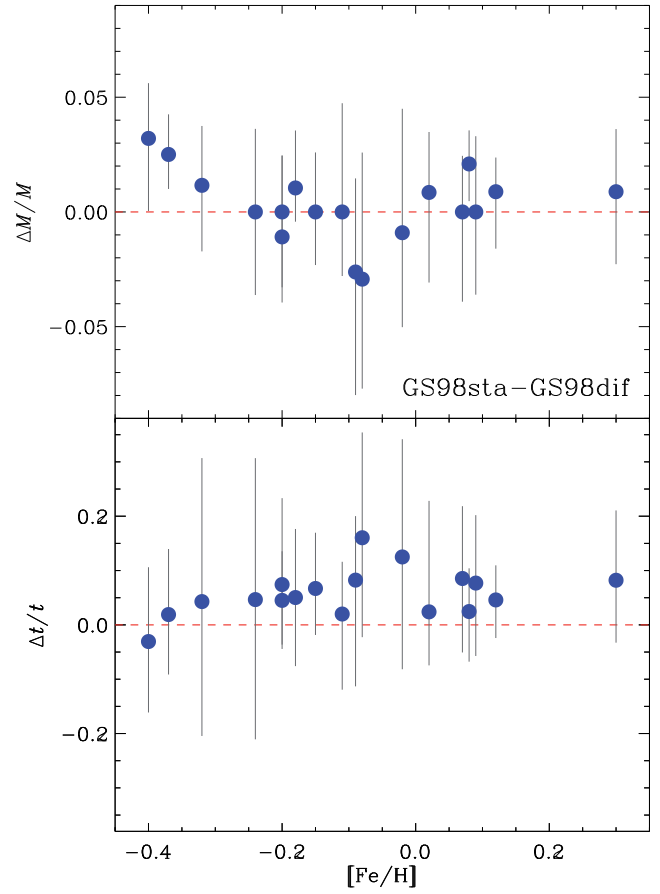
Figure 4. Fractional differences in mass and age obtained from the standard and diffusion grids of models as a function of spectroscopic metallicity, in the sense (GS98sta-GS98dif) Top: mass comparison. Bottom: age comparison. See the text for details.

method using the overshooting grid (GS98ove) for all targets and compared the results to those from the standard set of models.

Fig. 6 shows the fractional difference in mass and age obtained from both grids for stars with masses above 1.1 $M_\odot$. In three targets (Kepler-145, KOI-974, and Kepler-21), the mass and age deviations can be attributed to the quality of the fits: the PDFs
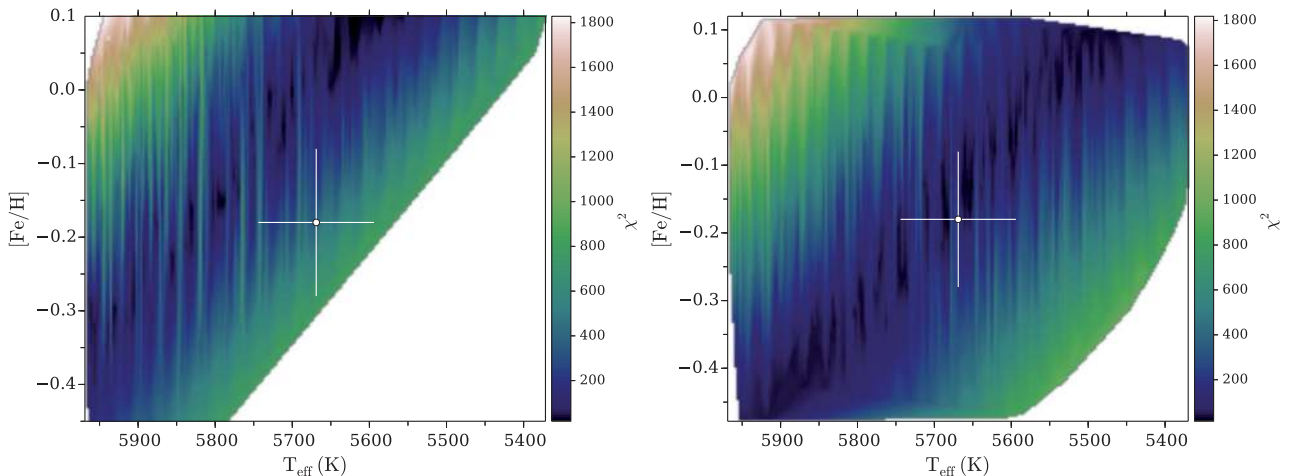

Figure 5. Values of χ^2 determined using the frequency ratios and spectroscopic constraints for Kepler-93. Solid lines depict the 1σ uncertainties in the spectroscopic atmospheric parameters. Left: standard grid. Right: diffusion grid.
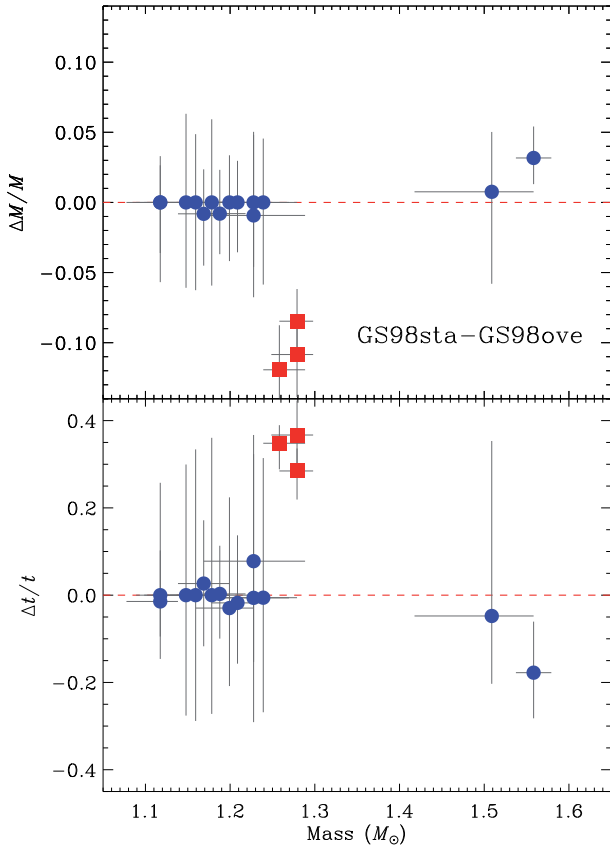
Figure 6. Fractional differences in mass and age obtained with the standard and overshooting grids as a function of stellar mass, in the sense (GS98sta-GS98ove) Top: mass comparison. Bottom: age comparison. Red squares show the positions of outliers Kepler-145, KOI-974, and Kepler-21. See the text for details.

Figure 7. Fractional mass difference between the standard and overshooting grids as a function of the TAMS ratio for the GS98sta grid. Red squares show the positions of outliers Kepler-145, KOI-974, and Kepler-21. The TAMS ratio is defined as the age of the best-fitting model in the GS98sta grid divided by the age at the end of the core hydrogen-burning phase. See the text for details.

Figure 8. Mass distribution obtained with BASTA for KOI-974 using the standard and overshooting grids.

of these particular stars show a clearly bimodal distribution (see below). A similar situation is observed in the target at $\sim$1.5 M$_\odot$, where the large mass and age uncertainty in the GS98sta results is a consequence of its Bayesian results encompassing the secondary peak in the distribution.

Besides the obvious outliers (red squares in Fig. 6), differences in the results are noticeable in five targets (HAT-P7, KOI-5, Kepler-50, Kepler-129, and KOI-288). Fig. 7 shows the fractional mass difference as a function of the TAMS ratio, defined as the ratio between the age of each target's best-fitting model and the age that model has when exhausting its central hydrogen content. The differences in mass appear at TAMS ratio values of $\sim$0.9 when convective cores are well developed and strongly influence the frequency ratios (Silva Aguirre et al. 2011a). Moreover, once the stars reach the turn-off at TAMS ratio of $\sim$1.0, some results are fully compatible while others still show small differences. This might be an indication of asteroseismic data keeping record of earlier mixing processes in stars once these have evolved slightly beyond the main-sequence phase (see Deheuvels & Michel 2011, where similar results were found). We note that for our targets with TAMS ratio larger than 1, their best-fitting models show evidence of mixed modes with no obvious counterparts in the observations, probably due to their low amplitudes.

The three outliers present in Figs 6 and 7 (Kepler-145, KOI-974, and Kepler-21) stem from bimodal probability distribution functions obtained from the GS98sta grid, which are not observed in the
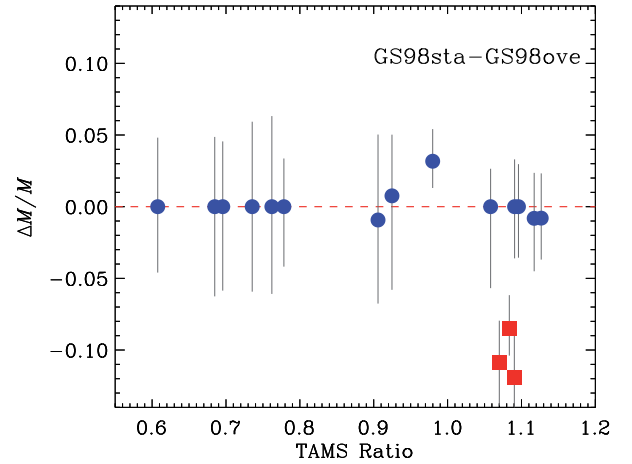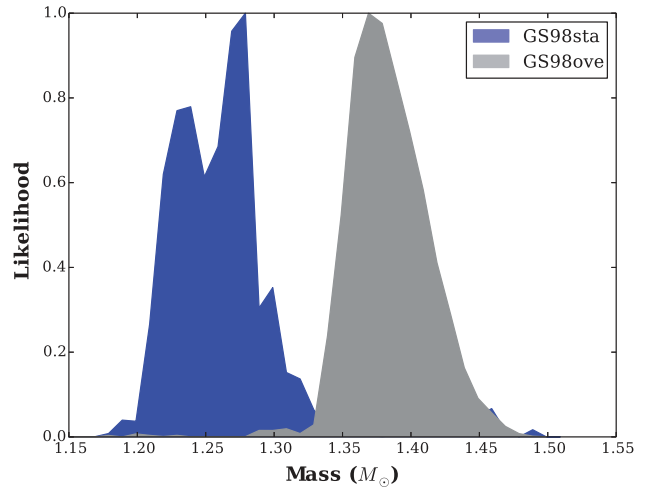
results when the GS98ove models are used instead. Fig. 8 shows the example of KOI-974, where the GS98sta grid favours a star with mass $\sim$1.27 M$_\odot$ that has evolved beyond the main sequence (TAMS $\sim$ 1.1; see Fig. 7). However, there is evidence of a secondary solution at higher masses, close to $\sim$1.43 M$_\odot$. When using the overshooting grid instead, the PDF shows a unique peak at $\sim$1.39 M$_\odot$ compatible with the high-mass solution seen in the GS98sta grid. A similar behaviour is observed in the PDFs for Kepler-145 and Kepler-21, where the GS98ove results favour masses consistent with the higher mass secondary peak in the GS98sta probability distribution function. We note that the bimodal nature of the solution for Kepler-21 had already been pointed out by Howell et al. (2012).

For the three outliers, the inclusion of overshooting produces a better fit to the frequency combinations and argues against the lower mass peak in the PDF. Since the GS98sta and GS98ove grids cover the same parameter space in terms of initial masses and compositions, we also compared the average likelihood of the grids for these targets and always found better agreement with the
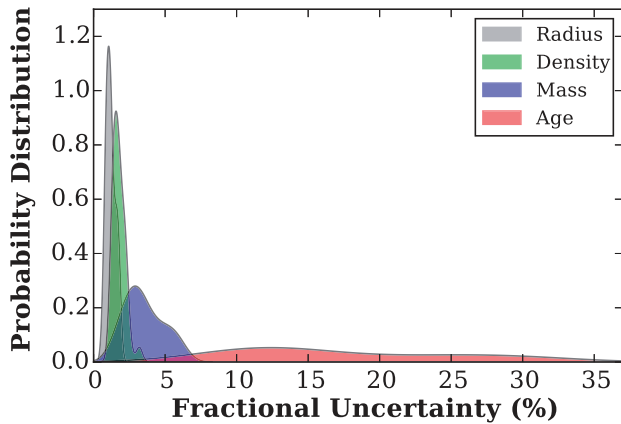
Figure 9. Fractional uncertainties added in quadrature in the final stellar parameters determined with our BASTA. See the text for details.

overshooting models. In fact, the GS98ove results in all three cases favour stars close to the end of the main-sequence phase (TAMS ~ 0.92), where convective cores are well developed and masses determined with the standard grid are slightly higher than with overshooting (see Fig. 7). Thus, the final parameters of these three KOIs, given in Table 3, are those determined from the GS98ove. This solution for Kepler-21 also results in a luminosity and a distance compatible with that determined from parallaxes, as described in Section 4.4 below. The actual mass value at which extending the convective core size by means of overshooting has an impact on the obtained properties is expected to be between 1.2 and 1.3 M$_\odot$, but the quality of the data and mass coverage of the current sample are not adequate to thoroughly test this transition. Figs 6 and 7 show that this reasonable expectation is consistent with the data.

Based on the analysis and comparisons on the input physics discussed in Sections 4.1.1 and 4.1.2, we choose the GS98dif grid to determine the final stellar properties and statistical uncertainties for stars of masses below $\sim$1.15 M$_\odot$, and the GS98ove grid for the remainder of the sample. These values are given in Table 3. In terms of internal precision, the median fractional uncertainties returned by the BASTA are 1.2 per cent (radius), 1.7 per cent (density), 3.3 per cent (mass), and 14 per cent (age). We note that the seemingly large fractional uncertainty on the density compared with asteroseismic determinations made by other methods arises from the use of frequency ratios instead of individual oscillation frequencies. The distributions for our sample shown in Fig. 9 correspond to the statistical uncertainties only. To check how robust this error budget is, we explore in the next sections the systematic contribution to the uncertainties from the input physics and fitting algorithms.

4.2 Systematic uncertainties from input physics

Our central recommended values and statistical uncertainties derived in the previous sections were based on fixed sets of input physics chosen according to our current best knowledge of stellar evolution (i.e. including microscopic diffusion and core overshooting in the relevant mass regimes). In this section, we explore the impact on our results from changing two quantities whose values are not yet fully constrained by observations or theory, namely the solar abundances and the mixing-length parameter.

The photospheric composition of the Sun has been revised in recent years inspired by the predictions of 3D model atmospheres (e.g. Asplund, Grevesse & Sauval 2005; Asplund et al. 2009;

Caffau et al. 2011). Although these hydrodynamical models of the solar atmosphere are much more realistic than the simple 1D atmospheres used by Grevesse & Sauval (1998), their results are not in agreement with the helioseismic determinations of the solar internal structure (e.g. Basu & Antia 2008; Christensen-Dalsgaard et al. 2009; Serenelli et al. 2009). Similarly, these simulations predict variations in the efficiency of convection as a function of $T_{\rm eff}$ and [Fe/H] (e.g. Magic, Weiss & Asplund 2015; Trampedach et al. 2014). In hydrostatic evolutionary models, this process is mimicked by the mixing-length theory and its efficiency is represented by one parameter ($\alpha_{\rm MLT}$) calibrated to reproduce the properties of the Sun.

A thorough analysis of the virtues of 3D model predictions compared to those of 1D models goes beyond the scope of this paper, but we are interested in knowing the impact of these results on our fitted stellar properties. For the case of the solar abundances, we have chosen to use the compilation of Asplund et al. (2009) since its determinations represent an extreme case with respect to those of Grevesse & Sauval (1998), while the results of Caffau et al. (2011) lie approximately in between these two determinations. In terms of convective efficiency, our standard grid uses a value calibrated to the solar properties; to test the impact of only changing $\alpha_{\rm MLT}$, we have computed grids with the Grevesse & Sauval (1998) abundances varying this parameter by ± 0.3, in agreement with the changes predicted by 3D simulations (see e.g. Trampedach et al. 2014). The resulting sets of models (AS09, GS98al+, GS98al−) are summarized in Table 1.

The stellar parameters obtained with BASTA and these three grids deviate systematically from the GS98sta results. When comparing to the values obtained with the Asplund et al. (2009) solar abundances, the median and standard deviation of the fractional differences are -0.1 ± 0.3 per cent (density), $+0.3 \pm 0.3$ per cent (radius), $+0.9 \pm 0.6$ per cent (mass), and $+4.0 \pm 3.3$ per cent (age). An increase in the mixing-length parameter on the other hand produces changes at the level of $+0.9 \pm 0.7$ per cent (density), -0.9 ± 0.6 per cent (radius), -2.4 ± 2.2 per cent (mass), and -0.2 ± 9.0 per cent (age), and of opposite sign if the $\alpha_{\rm MLT}$ value is decreased. Given that these differences are always smaller than the statistical errors quoted in the previous section, we have not added them to the error budget given in Table 3. We consider the dispersions as the major contribution to the uncertainties, and add them in quadrature[2] to quote a reference systematic effect arising from the difference in the input physics of 0.8 per cent (density), 0.7 per cent (radius), 2.3 per cent (mass), and 9.6 per cent (age).

4.3 Systematic uncertainties from fitting methods

As described in Sections 3.2 and 4.1, our recommended stellar properties are derived fitting the frequency ratios r_{010} and r_{02} and the spectroscopic parameters to two chosen grids of models depending on the mass range. In many asteroseismic analyses, it is customary to fit the individual mode frequencies (after applying a suitable surface correction) instead of frequency combinations. To isolate the impact of the choice of fitted seismic observables, we take advantage of the flexibility of BASTA in its input and compute stellar properties fitting the spectroscopic $T_{\rm eff}$ and [Fe/H] and the individual oscillation frequencies [corrected with the Kjeldsen et al. (2008) prescription]. The median fractional differences in the

---

[2] Giving the scatter from changing the mixing-length half the weight as its contribution is symmetric.

results obtained with BASTA+GS98sta using frequencies and ratios are below 0.5 per cent in density and radius, 1 per cent in mass, and 7 per cent in age. These values should be considered as a minimum set of systematic uncertainties based only on the choice of observables.

Applying the BASTA to one grid of GARSTEC models corresponds to a single determination of stellar properties at a fixed set of input physics, evolutionary code, pulsation code, and minimization technique. Throughout the years, several algorithms have been developed to reproduce asteroseismic data making use of a variety of stellar evolution and oscillation codes, considering different assumptions on the physics included and the treatment of the data to be fitted. We aim now at determining the systematic uncertainty arising from the use of different fitting pipelines, including the numerics of the evolution and pulsation codes as well as the minimization routine and chosen data sets.

Bearing this in mind, we have obtained results for our sample of KOIs using three different methods: the ASTEC Fitting (ASTFIT) method, the Yale Monte Carlo Method (YMCM), and the Asteroseismic Modeling Portal (AMP). To isolate the effects of using different codes and assumptions on data treatment, each algorithm has been applied using input physics as similar as possible to the standard GARSTEC grid (GS98sta), i.e. not including the effects of microscopic diffusion nor overshooting. Thus, all comparisons in this section are made between the results of these fitting algorithms and the BASTA+GS98sta combination. A description of the methods can be found in Appendix A, but we repeat here the main differences in each of the implementations with respect to the BASTA+GS98sta.

The ASTFIT method uses the ASTEC evolutionary code (Christensen-Dalsgaard 2008a) and was applied with the same physics as in the GS98sta grid (including a solar-calibrated mixing length and $\Delta Y / \Delta Z = 1.4$). Its main difference with respect to the BASTA is the asteroseismic variables to be fitted: instead of using frequency ratios, this algorithm matches the individual frequencies mimicking the surface effects via a scaled function determined from the frequency corrections found in the solar case (see Appendix A1 for details).

The YMCM differs from the BASTA+GS98sta combination in its evolution code (YREC; Demarque et al. 2008) and its pulsation code (first used in Antia & Basu 1994). Also, the assumptions on the initial composition are different: no helium-to-metal enrichment ratio is applied and the initial helium abundance is a free parameter in the minimization process. The stellar properties are obtained from a weighted average of the fit to the individual frequencies (with a solar-function correction for surface effects; see Appendix A2), the ratios, and the spectroscopic constraints. YMCM takes into account the correlations introduced by the construction of the frequency ratios (see equations 2 and 3).

In the case of the AMP, the evolution and pulsation codes are the same as in ASTFIT (Metcalfe, Creevey & Christensen-Dalsgaard 2009). However, its standard configuration adjusts both the mixing-length parameter and initial abundances when searching for the best-fitting model. The latter is found using a weighted average between the fit to the individual frequencies [corrected with the Kjeldsen et al. (2008) formulation], the frequency ratios r_{010} and r_{02}, and the spectroscopic constraints (see Appendix A3). Correlations are not taken into account in the frequency combinations and these are assumed to be independent.

Fig. 10 shows the fractional differences obtained in mean density and radius from the different methods. It is worth noticing that the YMCM could not provide a solution in four cases where the

best fit was found for helium abundances below the standard big bang nucleosynthesis (SBBN) value of $Y_0 = 0.248$. There is overall good agreement in the results, with the AMP values showing a larger scatter than the other two methods. The closest matches are obtained between the BASTA and ASTFIT, not surprisingly since these are computed with the exact same input physics. Median differences and standard deviations in densities and radii are below the ∼1 per cent level, while the comparison with the YMCM and AMP leads to median differences of the same order but a larger scatter (∼2 per cent). This shows remarkable level of agreement considering the variety of evolutionary and pulsation codes used as well as the treatment of asteroseismic data.

There is evidence of a metallicity dependence in the density and radius differences between the BASTA and YMCM results, while the comparison with the AMP does not suggest any correlation with the spectroscopic parameters. Similar features can be seen in Fig. 11, where the fractional differences in mass and age are shown. Once again there is excellent agreement between the BASTA and ASTFIT, with median and standard deviations in mass and age of 0.8 ± 2 per cent and 1.2 ± 9 per cent, respectively, and within the uncertainties in practically all cases. The previous trends with spectroscopic parameters remain with respect to the YMCM and AMP, namely a metallicity dependence in the first case and seemingly random scatter in the second one. This leads to mass estimates differing by up to ∼15 per cent and, via the mass–age correlation, to corresponding age differences of more than 40 per cent.

While the origin of these discrepancies will be explored in the following section, for the sake of the current analysis we use the scatter in the comparison between the BASTA and the ASTFIT results as a measurement of the systematic uncertainty arising purely from evolutionary codes and fitting methods, which conservatively accounts for 1 per cent in density and radius, 2 per cent in mass, and 9 per cent in age. This level of agreement is comparable to the one obtained with BASTA+GS98sta when changing the observables from ratios to individual frequencies, showing that remarkably precise determinations of stellar properties are possible from asteroseismology despite the use of different evolutionary codes as long as the considered input physics is kept as similar as possible.

4.4 Systematic uncertainties from the initial helium abundance

To understand now the origin of the discrepancies between YMCM, AMP, and the BASTA+GS98sta combination highlighted in the previous section, we naturally focus on the parameters that have been treated differently in the algorithms. The bottom panels in Fig. 12 show the fractional mass difference as a function of the difference in the initial helium abundance. In both cases, a correlation between $\Delta M/M$ and ΔY_{ini} can be seen, with higher masses predicted by the YMCM and AMP for lower values of the initial helium fraction. A similar trend can be seen when comparing the luminosities (middle panels in Fig. 12), which turns out to be a consequence of the different weights each fitting method gives to the spectroscopic constraints (see Appendix A and Section 3.2 for details).

Since there is good agreement in the median density and radii determined by all pipelines (better than 2 per cent with a larger scatter for AMP), differences in luminosity arise from differences in effective temperature of each model. The top panels of Fig. 12 show the match to the spectroscopic T_{eff} value predicted by each algorithm, revealing very close agreement between these codes and the spectra (mean difference of 20 and 35 K for AMP and YMCM, respectively). ASTFIT and the BASTA on the other hand predict
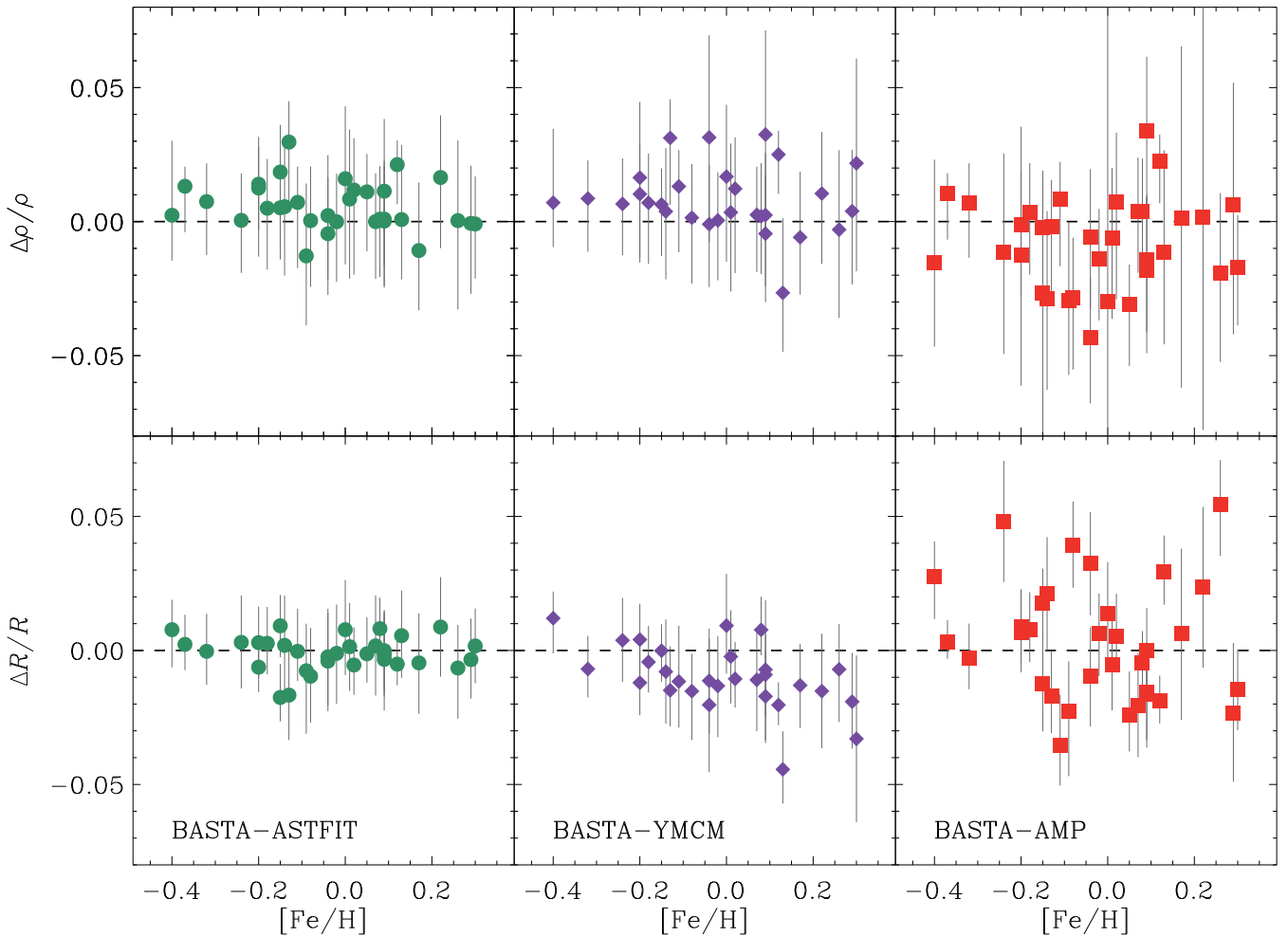
Figure 10. Fractional differences in stellar density and radius for the three fitting methods compared to the BASTA results as a function of spectroscopic metallicity, given as (BASTA-other).

$T_{\rm eff}$ values systematically higher than the spectroscopic ones at a level of ~45 and 70 K, respectively. The reason for this difference is that the AMP and YMCM have the flexibility to fit $T_{\rm eff}$ at a fixed radius by changing the luminosity via its strong dependence on the molecular weight and thus the helium abundance. Our final results from the BASTA given in Table 3 do not suffer from this systematic offset in $T_{\rm eff}$ as they include microscopic diffusion which effectively compensates for this effect as shown in Fig. 5 (see also discussion in Section 4.1).

The initial helium abundance in low- and intermediate-mass stars is a poorly constrained quantity as helium lines are not detectable in their spectra. Usually, these abundances are computed assuming a linear enrichment law $\Delta Y/\Delta Z$ anchored to primordial values (Y_0, Z_0) determined from SBBN or a solar calibration. The actual slope of the relation has been determined from different sources such as low-main-sequence stars in the solar neighbourhood (Jimenez 2003; Casagrande et al. 2007), galactic and extragalactic H II regions (Balser 2006), and stellar evolution theory for a given initial mass function (e.g. Chiappini, Renda & Matteucci 2002). There is no consensus yet on the relation being linear across all metallicity values or the slope changing for different types of stars and metallicity ranges. However, there is broad agreement on the expected range for the relation being within $1 \leq \Delta Y/\Delta Z \leq 3$ (except for some very peculiar objects such as ω Centauri; see Norris 2004). Depending

on the chosen solar composition, determination of the initial helium abundance of the Sun agrees with a slope of $1.7 \leq \Delta Y/\Delta Z \leq 2.2$ (see Serenelli & Basu 2010).

Fig. 13 compares the predictions of helium-to-metal enrichment laws of different slopes with the initial abundances determined by the YMCM and AMP. We remind the reader that the BASTA and ASTFIT results are anchored to $\Delta Y/\Delta Z = 1.4$ and therefore follow a straight line if plotted in the figure. As expected, a large majority of the YMCM results lie below this line and in many cases very close to the primordial SBBN value which was used as a hard edge in the modelling procedure. The AMP results on the other hand only force a hard cut in $Y_{\rm ini} = 0.22$ and show a much larger scatter as well as five targets with initial helium abundances below the SBBN line. This occurs for stars both at low metallicities and at and above the solar value ($Z_{\rm ini} \sim 0.018$). The AMP also predicts high initial helium for stars of metallicity lower than the Sun, which occurs only for one case in the YMCM results.

Only two of our targets have available *Hipparcos* parallaxes from Van Leeuwen (2007): Kepler-21 ($\pi = 8.86 \pm 0.58$ mas) and KOI-3158 ($\pi = 28.03 \pm 0.82$ mas). Using the asteroseismic log g value and spectroscopic metallicity, we applied the infrared flux method (IRFM; see Section 4.5) to determine the bolometric flux and the luminosity of the stars. The resulting values of $L/L_\odot = 5.54 \pm 0.78$ (Kepler-21) and $L/L_\odot = 0.38 \pm 0.03$ (KOI-3158) are compatible
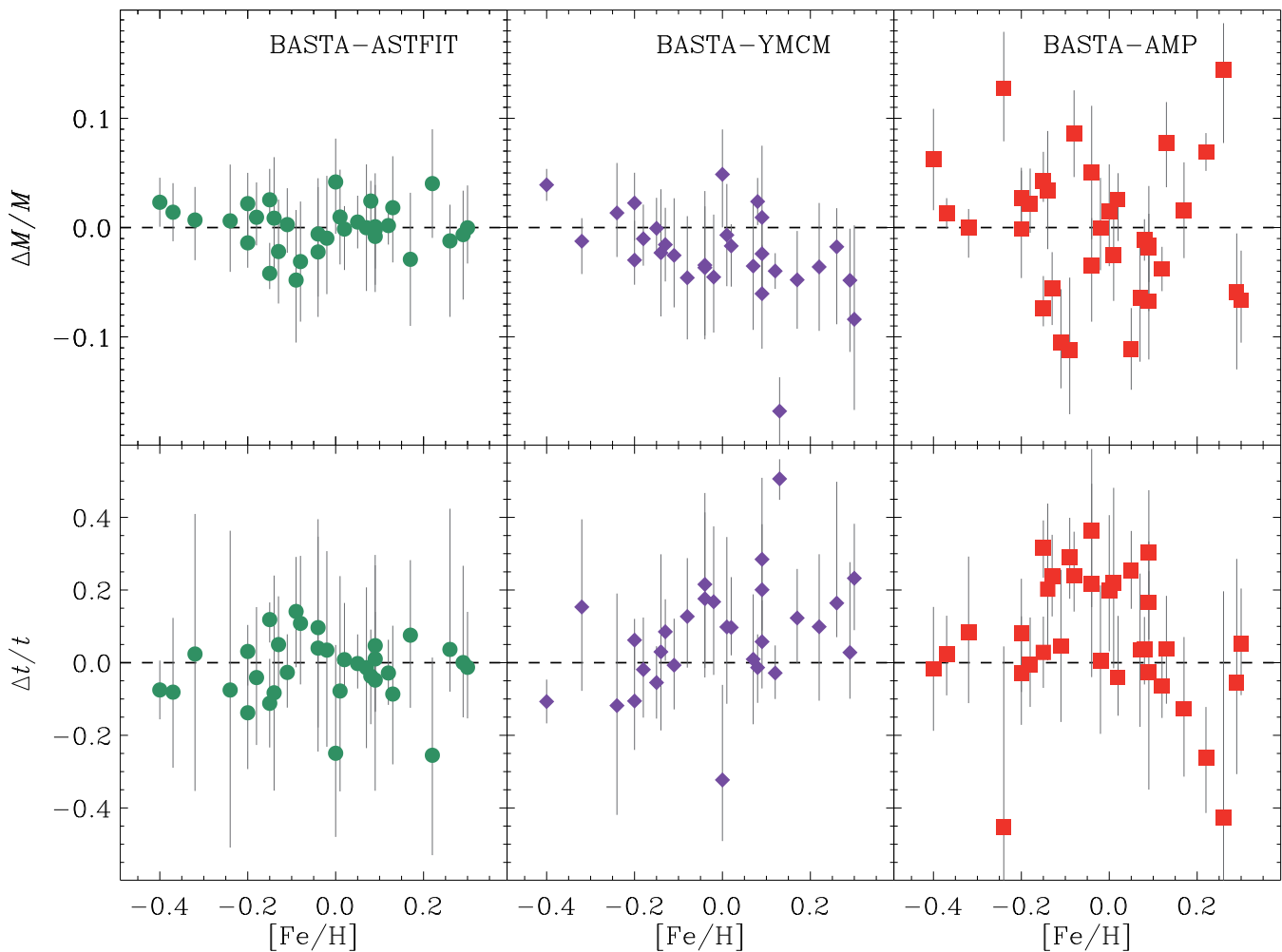
Figure 11. Fractional differences in stellar mass and age for the three fitting methods compared to the BASTA results as a function of spectroscopic metallicity, given as (BASTA-other).

with those determined with the BASTA (see Table 3). ASTFIT predicts the correct luminosity for KOI-3128 ($L/L_\odot = 0.35 \pm 0.02$) while its determination for Kepler-21 results in a slightly lower value than observed ($L/L_\odot = 4.59 \pm 0.11$). The reason for this discrepancy is that ASTFIT favours the low-mass solution in the bimodal mass distribution observed for Kepler-21 (see Section 4.1); the final results of the BASTA are based on the overshooting grid that favours a higher mass value. For comparison, the low-mass solution obtained with the BASTA+GS98sta predicts a luminosity of $L/L_\odot = 4.80^{+0.12}_{-0.10}$.

The results from AMP return similar luminosities as ASTFIT: $L/L_\odot = 0.36 \pm 0.02$ (KOI-3158) and $L/L_\odot = 4.37 \pm 0.19$ (Kepler-21). However, in both cases, the Y_{ini} values from AMP are slightly below the SBBN one: the luminosity of KOI-3158 is still well reproduced because at such low metallicities the initial helium abundance at $\Delta Y/\Delta Z = 1.4$ is not very different from the primordial one ($Y_{ini} \sim 0.258$). The resulting mass of Kepler-21 is higher than that from ASTFIT but the luminosity is lower as a consequence of the difference in initial helium abundance at compositions closer to solar ($Y_{ini} \sim 0.270$).

The correlation between mass and helium abundance severely affects asteroseismically derived stellar properties (see section 4.3 in Lebreton & Goupil 2014), and has recurrently appeared in studies fitting individual frequencies (e.g. Mathur et al. 2012; Metcalfe

et al. 2014). Assessing if the sub-SBBN results have astrophysical meaning goes beyond the scope of this paper, but the dependence on helium abundance of asteroseismic solutions needs to be further investigated and thoroughly understood. In order to estimate an uncertainty arising from the changes in initial helium content, we compare the results of BASTA, YMCM, and AMP for the subset of targets falling within the expected range of $1 \leq \Delta Y/\Delta Z \leq 3$. There are five and nine targets fulfilling this criterion in the YMCM and AMP results, respectively (see Fig. 13). The average standard deviations around the median of the results are 1.6 per cent (radius), 1.7 per cent (density), 3.6 per cent (mass), and 16.8 per cent (age). These uncertainties are comparable to the statistical ones obtained with BASTA+GARSTEC grids, as described at the end of Section 4.1.

In an initial attempt to solving the issue of asteroseismic analysis favouring sub-SBBN helium models, we consider the correlation of properties with initial helium abundances shown in Fig. 12. Our results for the two targets where parallax-derived luminosities are available suggest better agreement with grids computed assuming $\Delta Y/\Delta Z = 1.4$, although the uncertainties are still rather large and AMP results are only slightly more than 1σ away in Kepler-21. We expect much tighter observational constraints on the luminosity from the *Gaia* mission that will essentially translate into a constraint on Y_{ini}, breaking the degeneracy and subjecting the $\Delta Y/\Delta Z$ relation to an additional test from asteroseismology.
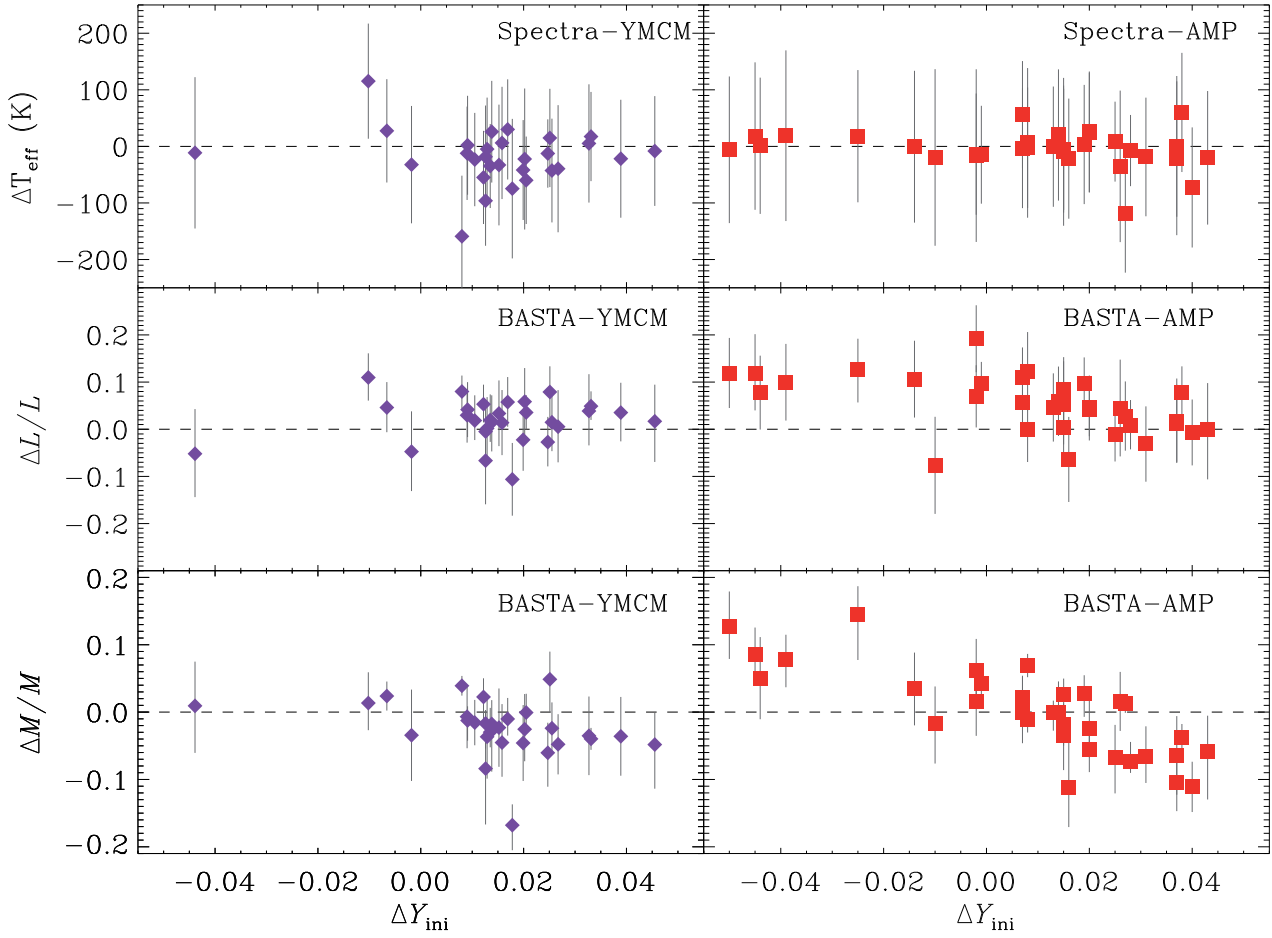
Figure 12. Comparison of stellar properties as a function of the difference in the initial helium abundance, given as (BASTA-code). Top panels: difference in effective temperature between the spectroscopically measured one and that extracted from the fitting methods. Middle panels: fractional differences in the luminosities predicted by the codes. Bottom panels: fractional mass differences between codes. See the text for details.
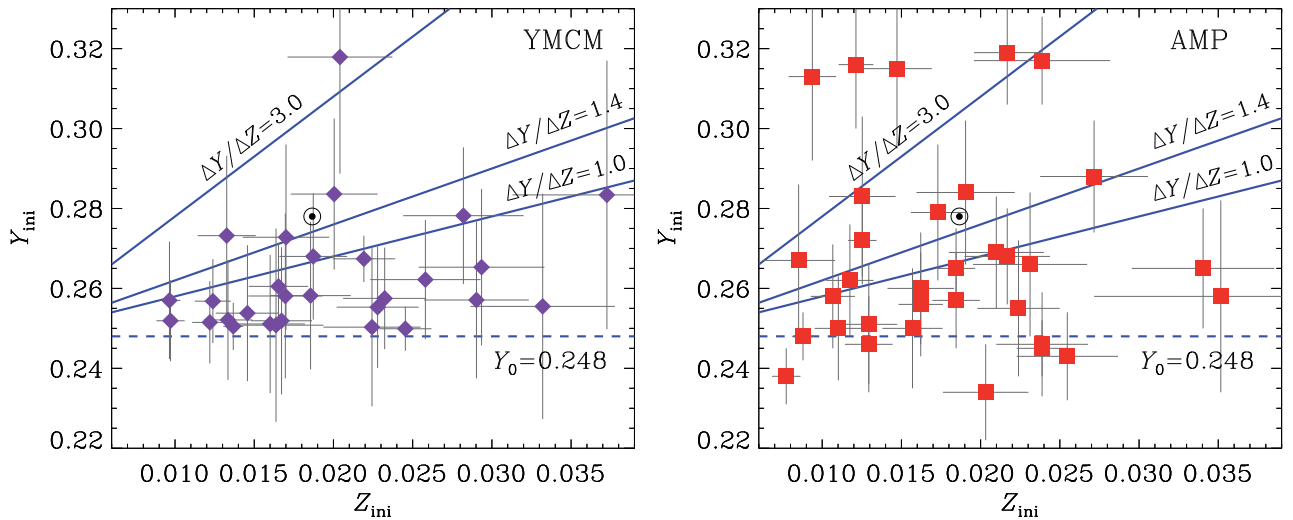

Figure 13. Initial metallicity versus initial helium abundance for the results determined by two different codes. Horizontal dashed lines show the primordial helium abundance predicted by SBBN, while solid lines depict different galactic enrichment laws anchored to $Y_0 = 0.248$ and $Z_0 = 0$. Solar symbol depicts the initial solar abundance from Serenelli & Basu (2010). Left: YMCM. Right: AMP. See the text for details.

4.5 Distances

We have determined distances to our targets combining the results of the IRFM (Casagrande et al. 2010) with asteroseismically determined stellar parameters (Silva Aguirre et al. 2011b). This technique has been shown to provide accurate *Hipparcos*-quality distances for individual targets (Silva Aguirre et al. 2012) and has been recently applied to the first galactic archaeology study of the *Kepler* field (Casagrande et al. 2014).

In its current implementation, the method relies on multi-band *griz* photometry from the original Kepler Input Catalogue (KIC; Brown et al. 2011), *JHK*$_S$ magnitudes from 2MASS, and the spectroscopically determined metallicity to recover the bolometric flux as a function of surface gravity. The precise log *g* values obtained from asteroseismology are included in an iterative process until convergence in reddening and effective temperature is achieved (see section 3 in Silva Aguirre et al. 2012, for details).

Unfortunately, only 22 of our 33 targets have reliable KIC photometry taken in all *griz* filters, and we have initially determined distances for this subsample using the combination of the IRFM and asteroseismology. With the aim of providing a complete and homogeneous set of stellar distances for the full cohort, we have used the *J* − *K*$_S$ angular diameter calibration of Casagrande, Portinari & Flynn (2006) to obtain distances to all targets, and compared them to the full IRFM results. For the 22 targets, the median and standard deviation of the fractional distance difference between both determinations are 0.3 ± 5.1 per cent, showing that the calibration works well for the selected sample. The distances given in Table 3 for all targets have been determined from the colour–angular diameter calibration, and have a fractional median uncertainty of 4.4 per cent.

The two stars in our sample with measured *Hipparcos* parallaxes allow for an independent check on our distances. The resulting values of *d* = 112.9 ± 7.4 pc for Kepler-21 and *d* = 35.7 ± 1.04 pc for KOI-3158 are compatible within their uncertainties to those determined by our method (114 and 33 pc, respectively, see Table 3).

5 COMPARISON WITH ASTEROSEISMIC SCALING RELATIONS

The analysis presented in the previous sections has been possible for a subsample of almost half the currently studied KOIs where asteroseismic data are available. In the rest, SNRs are too low or the frequency resolution not sufficiently high to robustly extract individual oscillation frequencies (see e.g. Chaplin et al. 2014). Under these circumstances, asteroseismic determination of stellar parameters is carried out based on the properties of the readily extractable average global parameters $\langle \Delta \nu \rangle$ and ν_{max}. The former quantity is a proxy of the mean stellar density $\bar{\rho}$ (Ulrich 1986), while the latter has been shown to scale with the surface gravity and effective temperature (Brown et al. 1991; Kjeldsen & Bedding 1995; Bedding & Kjeldsen 2003):

$$\left(\frac{\langle \Delta \nu \rangle}{\langle \Delta \nu_{\odot} \rangle} \right)^2 \simeq \frac{\bar{\rho}}{\bar{\rho}_{\odot}} , \tag{11}$$

$$\frac{\nu_{max}}{\nu_{max,\odot}} \simeq \frac{M}{M_{\odot}} \left(\frac{R}{R_{\odot}} \right)^{-2} \left(\frac{T_{eff}}{T_{eff,\odot}} \right)^{-1/2} . \tag{12}$$

Here, $\bar{\rho}_{\odot}$ and $T_{eff,\odot}$ correspond to the solar properties. Consequently, $\langle \Delta \nu \rangle$ and ν_{max} are the basis of the asteroseismic scaling relations

$$\frac{M}{M_{\odot}} \simeq \left(\frac{\nu_{max}}{\nu_{max,\odot}} \right)^3 \left(\frac{\langle \Delta \nu \rangle}{\langle \Delta \nu_{\odot} \rangle} \right)^{-4} \left(\frac{T_{eff}}{T_{eff,\odot}} \right)^{3/2} , \tag{13}$$

$$\frac{R}{R_{\odot}} \simeq \left(\frac{\nu_{max}}{\nu_{max,\odot}} \right) \left(\frac{\langle \Delta \nu \rangle}{\langle \Delta \nu_{\odot} \rangle} \right)^{-2} \left(\frac{T_{eff}}{T_{eff,\odot}} \right)^{1/2} , \tag{14}$$

where $\langle \Delta \nu_{\odot} \rangle$ and $\nu_{max,\odot}$ are the solar values as determined by the same method used to analyse the data.

When a determination of T_{eff} is available, equations (13) and (14) provide masses and radii independent of any stellar models (e.g. Stello et al. 2008; Silva Aguirre et al. 2011b). Coupled to evolutionary tracks, the asteroseismic scaling relations can also provide an age estimation via the so-called grid-based method, which matches the spectroscopic constraints and measured $\langle \Delta \nu \rangle$ and ν_{max} to the same values predicted from stellar models (e.g. Basu, Chaplin & Elsworth 2010; Gai et al. 2011; Lundkvist, Kjeldsen & Silva Aguirre 2014; Silva Aguirre et al. 2014). These techniques have been extensively used in characterization of the *CoRoT* and *Kepler* samples (e.g. Mosser et al. 2010; Huber et al. 2014), studies of open clusters (e.g. Basu et al. 2011; Stello et al. 2011), galactic archaeology (e.g. Miglio et al. 2013b; Casagrande et al. 2014), and will form the basis of asteroseismic analysis for the vast majority of targets observed by the repurposed *Kepler* mission (*K2*; Howell et al. 2014).

The $\langle \Delta \nu \rangle$ relation in equation (11) has direct theoretical foundation while the ν_{max} scaling in equation (12) is mostly an empirical relation (although see Belkacem et al. 2011). For these reasons, the asteroseismic scaling relations need to be thoroughly tested and calibrated, and have been the subject of scrutiny in the past few years. Studies have shown that radii of main-sequence stars predicted from asteroseismology agree with determinations from parallaxes and interferometry (e.g. North et al. 2007; Bedding et al. 2010; Miglio 2011; Huber et al. 2012; Silva Aguirre et al. 2012; White et al. 2013), while asteroseismic masses still remain to be confirmed by independent measurements. In the case of red giant stars, recent work has cautioned about the predictions from scaling relations in first ascent red giant and red clump stars (Miglio et al. 2012), expected masses of metal-poor stars (Epstein et al. 2014), and open cluster properties of main-sequence binaries (Brogaard et al. 2012; Miglio et al. 2012). Results from detailed modelling also suggest that the scaling relations underestimate the mean stellar density of red giant stars by ∼5 per cent (Huber et al. 2013a).

While acknowledging the shortcomings of our current understanding of the physics behind equations (11) and (12), we note that the discrepancies arise in regimes of metallicity and evolutionary state far from the main sequence for middle-aged stars near the mass of our Sun from where these relations are extrapolated. Our sample of KOIs presents an opportunity to compare determinations from individual frequencies with those of the grid-based method in a parameter space closer to the Sun, and thus to validate the results of the scaling relations for population studies in this region of the Hertzsprung–Russell diagram. The BASTA presented in Section 3.2 is flexible and can be adapted to any set of input data. We include as observational constraints the quantities T_{eff}, [Fe/H], $\langle \Delta \nu \rangle$, and ν_{max} of each target, which have been determined by Huber et al. (2013b). To derive their stellar properties, we need to determine ν_{max} and $\langle \Delta \nu \rangle$ in stellar evolution models.
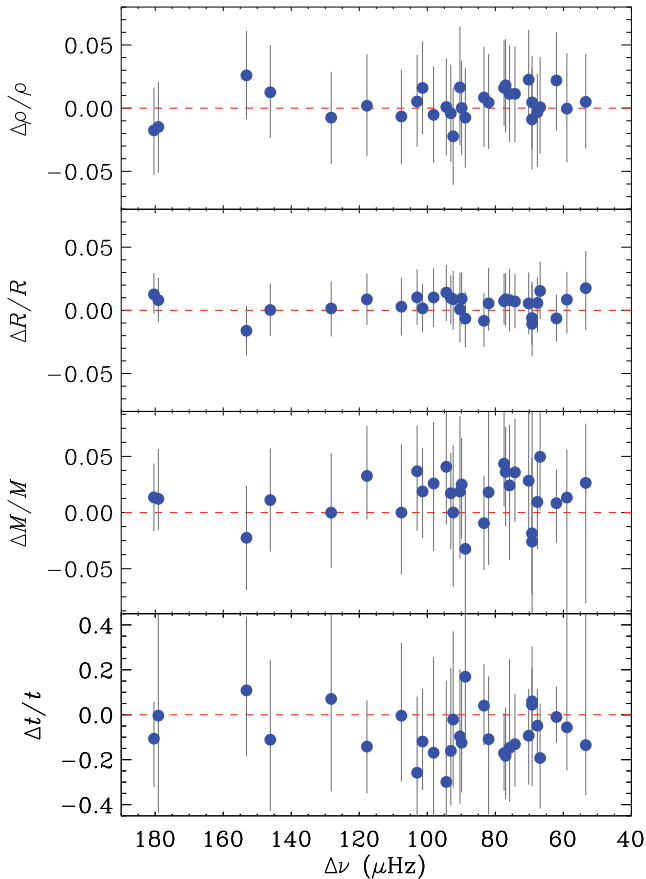
Figure 14. Fractional differences in stellar properties determined from the frequency combinations and the scaling relations as a function of the large frequency separation, in the sense (combinations-scaling).

The theoretical ν_{max} value can only be obtained using equation (12), and we adopt for the reference solar value entering this equation $\nu_{max,\odot} = 3090 \pm 30\,\mu Hz$ given by Huber et al. (2011). The theoretical $\langle \Delta\nu \rangle$ on the other hand can be obtained either from equation (11) or directly from the individual frequencies of oscillations calculated for each stellar model. To implement the latter approach, we must take into account the way $\langle \Delta\nu \rangle$ is estimated from the observed frequencies and treat models and data as similarly as possible (see White et al. 2011). With this in mind, we adopt the following procedure: we determine the theoretical $\langle \Delta\nu \rangle$ using a Gaussian-weighted linear fit to the $\ell = 0$ modes of each model as a function of radial order n, centred at the ν_{max} value obtained from equation (12) and with a width of 0.25 ν_{max}.

Fig. 14 shows the comparison between the stellar properties determined with the BASTA in Section 4 using the frequency ratios and those obtained using the global asteroseismic parameters, where $\langle \Delta\nu \rangle$ in the models has been computed using the aforementioned Gaussian fit to the theoretical frequencies. There are three outliers (same as in Section 4.1.2, not shown in this figure) corresponding to stars presenting bimodal PDFs. For the rest of the sample, there is excellent agreement between both determinations, with median fractional differences and standard deviations of 0.5 ± 1.2 per cent (density), 0.7 ± 0.8 per cent (radius), 1.8 ± 2.1 per cent (mass), and -10.6 ± 10.8 per cent (age). These results are reassuring considering that median uncertainties in grid-based determinations are usually of the order of 2.2 per cent in radius, 2.8 per cent in density, 5.4 per cent in mass, and 25 per cent in age (Chaplin et al. 2014).

Thus, stellar properties in the T_{eff} and [Fe/H] regime explored obtained from the global average asteroseismic parameters are compatible with those from individual frequency determinations and can be used when the latter are not available.

Finally, we have computed a set of stellar properties for our KOI sample using the two scaling relations (equations 11 and 12) to determine the global asteroseismic parameters, and the Huber et al. (2011) reference solar values ($\langle \Delta\nu_\odot \rangle = 135.1 \pm 0.1\,\mu Hz$, $\nu_{max,\odot} = 3090 \pm 30\,\mu Hz$). The median fractional differences and standard deviations with the results obtained from frequency combinations are -1.7 ± 1.2 per cent (density), 1.5 ± 0.9 per cent (radius), 2.6 ± 2.2 per cent (mass), and -10.4 ± 11.5 per cent (age). The level of agreement is slightly worse than that obtained when the theoretical $\langle \Delta\nu \rangle$ was computed from individual frequencies, but still well within the median uncertainties of the method quoted by Chaplin et al. (2014). However, compared to the results from the frequency ratios, the differences are of systematic nature with the scaling relations overestimating the density and underestimating the radius and mass. Departures from the $\langle \Delta\nu \rangle$ scaling relation (equation 11) in stellar models can introduce biases in the results, and have already been reported by White et al. (2011) and Chaplin et al. (2014) in the main-sequence phase. A detailed exploration of this systematic biases goes beyond the scope of this study and will be addressed in a subsequent publication.

6 AGE CORRELATIONS WITH EXOPLANET PROPERTIES

Using the stellar properties determined with the BASTA and shown in Table 3, we can investigate the distribution of planetary properties such as orbital period, radius, and multiplicity as a function of stellar age. Fig. 15 illustrates the age distribution of our sample as a function of planet radius and orbital period, showing that the majority of the high-SNR asteroseismic host stars are older than the Sun. Also, two main populations can be distinguished in age, at ~3 and ~6 Gyr. These features arise due to biases in the detection of stellar pulsations, whose amplitudes are proportional to the stellar luminosity (e.g. Kjeldsen & Bedding 1995). The net result is that detections are favoured in F-type (with ages about 2–3 Gyr) and old G-type (i.e. 6 Gyr) stars that have high enough luminosities (see e.g. fig. 1 in Silva Aguirre et al. 2011b). Given these age biases for high signal-to-noise asteroseismic detections, it should not be inferred that our finding of an average age greater than solar applies to either the *Kepler* exoplanet host-star sample in general, or the larger set of all *Kepler* dwarf stars comprising the exoplanet search programme. However, it is interesting to look for age correlations using this sample and explore the future prospects for larger samples of asteroseismically determined stellar properties of host stars.

Fig. 15 shows no obvious trends of stellar age with planet radii or orbital periods. This is not surprising given that evolutionary effects which are expected to affect planet radii or orbital periods such as photoevaporation and orbital migration are expected to occur within <1 Gyr (Lin, Bodenheimer & Richardson 1996; Lopez & Fortney 2013), and our sample does not contain such young stars. Nevertheless, our sample suggests that the period and radius distribution appears to be approximately constant for ages >2 Gyr, and hence is likely representative for Sun-like host stars observed by *Kepler*. We also do not detect any significant difference in the multiplicity fraction between young (~2–4 Gyr) and old (>5 Gyr) stars.

Finally, Fig. 16 shows the ratio of planetary periods for all known multiple systems in our sample. Studies of the larger *Kepler*
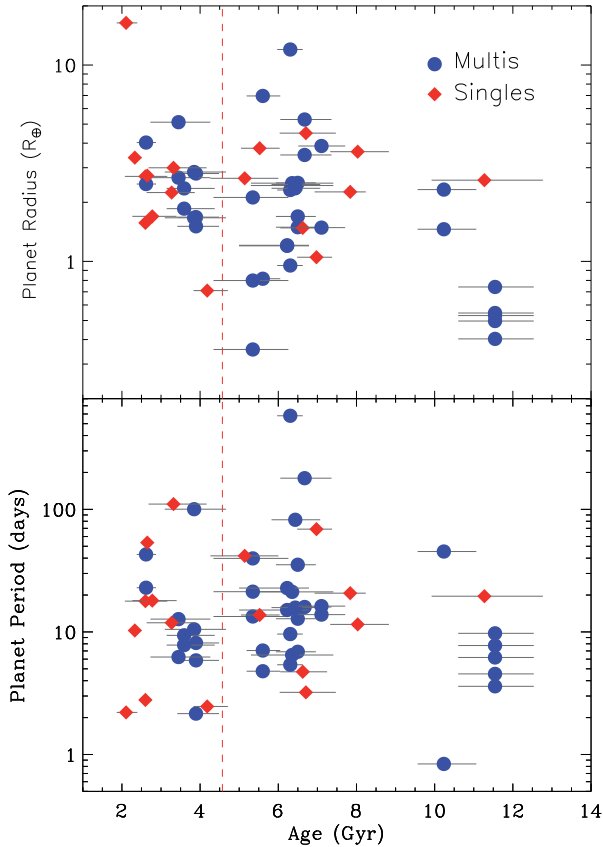
Figure 15. Properties of single (red diamonds) and multiple (blue circles) systems as a function of stellar age. Top panel: planetary radius. Bottom panel: planetary period. The oldest multiple system corresponds to the five planets detected around KOI-3158. Vertical dashed line marks the solar.
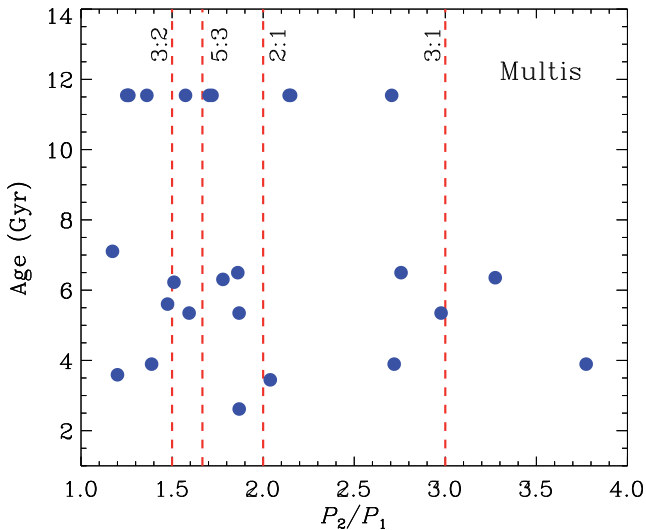

Figure 16. Period ratios for the multiple systems in our sample. Dashed lines mark the 3:2, 5:3, 2:1, and 3:1 mean-motion resonances.

planet-candidate sample have shown that most planets are not on exact resonant orbits, but that their period ratios tend to be near first-order resonances (e.g. Fabrycky et al. 2014). Although our sample is small, the results seem to indicate that these conclusions hold independently of the age of the host stars.

7 CONCLUSIONS

We have made use of the full time-base of observations from the *Kepler* satellite to uniformly determine precise fundamental stellar parameters, including ages, for a sample of exoplanet host stars where high-quality asteroseismic data were available. We devised a Bayesian procedure flexible in its input and applied it to different grids of models to study systematics from input physics and extract statistically robust properties for all stars. Our main results can be summarized as follows.

(1) The stellar properties determined from each grid of models reflect the impact of the input physics in asteroseismic studies. The inclusion of microscopic diffusion clearly affects the ages derived while providing better fits to the spectroscopically determined effective temperature and metallicity. Extending the convective core size by means of overshooting results in slightly less massive stars than the standard Schwarzschild case once the convective core is well developed and the target is close to the TAMS. Interestingly, we show that including this effect favours a particular solution when bimodal distributions in mass are present.

(2) Our results show that statistical uncertainties are below 2 per cent in radius and density, ∼3 per cent in mass, ∼4.5 per cent in distance, and ∼14 per cent in age. This level of precision is perfectly suited for supporting characterization of exoplanet systems, including determination of eccentricities by comparison of stellar densities from transit measurements with asteroseismic ones (e.g. Fogtmann-Schulz et al. 2014; Van Eylen et al. 2014). Furthermore, our catalogue of stellar ages can be used for studying time evolution of planetary systems, tidal interactions, and circularization time-scales.

(3) We have tested the systematic uncertainties introduced by changing the solar abundances and the efficiency of convection, and found them to be smaller than the statistical errors. We explored the impact on the stellar properties of reproducing different sets of asteroseismic observables (individual frequencies or frequency combinations), using different evolutionary and pulsation codes, as well as fitting algorithms, and found that when the input physics is kept the same the systematic differences are of the order of 1 per cent in density and radius, and 2 per cent and 9 per cent in mass and age. A source of uncertainty comparable to the statistical ones comes from the relation between metallicity and initial helium (Y_{ini}), and we expect the *Gaia* results to produce determinations of luminosity and provide an independent constraint on the initial helium abundances. Fitting algorithms that do not restrict this parameter commonly predict too low values of the Y_{ini}, even below SBBN. In Kepler-21, where a parallax measurement is available, the obtained luminosity of the sub-SBBN model is 1.5σ away from the parallax inferred value.

(4) When the SNR of the data is too low and individual frequencies of oscillation are not possible to extract, asteroseismic determination of stellar properties is made using the global asteroseismic parameters. We have applied the BASTA using these observables and the spectroscopic constraints as input and found excellent agreement with properties determined from frequency combinations. These results validate the use of the global asteroseismic observables in the regime explored in this paper when the theoretical value of $\langle \Delta \nu \rangle$ is computed from individual frequencies of oscillations. If determined from the scaling relation instead, the results should be treated with caution as they seem to overestimate the density and underestimate the mass and radius.

(5) Our results further demonstrate the positive synergy between asteroseismology and exoplanet studies, with the added ingredient

of precise age determinations to a level better than 15 per cent. We have investigated age correlations with planetary period and radii in our sample, finding no noticeable trend in the results. Their distribution as a function of age appears constant and is likely representative of the underlying population of *Kepler* Sun-like host stars. In terms of resonances, our findings suggest that the period ratios in multiple systems tend to be near first-order resonances regardless of the age of the system. Although subject to selection biases, our sample shows that the majority of planet host stars with asteroseismic observations of high SNR are older than the Sun.

The results presented here will provide the basis of upcoming catalogues of asteroseismic properties of exoplanet host stars, where over 100 KOIs with $\langle \Delta \nu \rangle$ and ν_{max} measurements will be characterized (Huber et al., in preparation). This larger sample will extend the investigation we have initiated in this paper on the dependence of planetary properties with the age of the host star. Similarly, the BASTA combined with grids of evolutionary models will provide stellar properties for targets observed by the *TESS* and *PLATO* missions in evolutionary stages beyond the main-sequence phase.

REFERENCES

Aerts C., Christensen-Dalsgaard J., Kurtz D. W. eds 2010, Asteroseismology. Springer-Verlag, Heidelberg
Aizenman M., Smeyers P., Weigert A., 1977, A&A, 58, 41
Angulo C. et al., 1999, Nucl. Phys. A, 656, 3
Antia H. M., Basu S., 1994, A&AS, 107, 421
Appourchaux T. et al., 2012, A&A, 543, A54
Arentoft T. et al., 2008, ApJ, 687, 1180
Asplund M., Grevesse N., Sauval A. J., 2005, in Barnes T. G., III Bash F. N., eds, ASP Conf. Ser. Vol. 336, Cosmic Abundances as Records of Stellar Evolution and Nucleosynthesis in Honor of David L. Lambert. Astron. Soc. Pac., San Francisco, p. 25
Asplund M., Grevesse N., Sauval A. J., Scott P., 2009, ARA&A, 47, 481
Ballard S. et al., 2014, ApJ, 790, 12
Balser D. S., 2006, AJ, 132, 2326
Barclay T. et al., 2013, Nature, 494, 452
Basu S., Antia H. M., 2008, Phys. Rep., 457, 217
Basu S., Chaplin W. J., Elsworth Y., 2010, ApJ, 710, 1596
Basu S. et al., 2011, ApJ, 729, L10
Batalha N. M. et al., 2011, ApJ, 729, 27
Bedding T. R., Kjeldsen H., 2003, Publ. Astron. Soc. Aust., 20, 203
Bedding T. R. et al., 2010, ApJ, 713, 935
Belkacem K., Goupil M. J., Dupret M. A., Samadi R., Baudin F., Noels A., Mosser B., 2011, A&A, 530, 142
Benomar O., Bedding T. R., Stello D., Deheuvels S., White T. R., Christensen-Dalsgaard J., 2012, ApJ, 745, L33
Benomar O., Masuda K., Shibahashi H., Suto Y., 2014, PASJ, 66, 94
Borucki W. J. et al., 2010, Science, 327, 977
Bouchy F., Carrier F., 2001, A&A, 374, L5
Brogaard K. et al., 2012, A&A, 543, A106
Brown T. M., Gilliland R. L., Noyes R. W., Ramsey L. W., 1991, ApJ, 368, 599
Brown T. M., Latham D. W., Everett M. E., Esquerdo G. A., 2011, AJ, 142, 112
Caffau E., Ludwig H.-G., Steffen M., Freytag B., Bonifacio P., 2011, Sol. Phys., 268, 255
Campante T. L. et al., 2014, ApJ, 783, 123
Campante T. L. et al., 2015, ApJ, 799, 170
Carrier F., Eggenberger P., Bouchy F., 2005, A&A, 434, 1085
Carter J. A. et al., 2012, Science, 337, 556
Casagrande L., Portinari L., Flynn C., 2006, MNRAS, 373, 13
Casagrande L., Flynn C., Portinari L., Girardi L., Jimenez R., 2007, MNRAS, 382, 1516
Casagrande L., Ramírez I., Meléndez J., Bessell M., Asplund M., 2010, A&A, 512, 54
Casagrande L. et al., 2014, ApJ, 787, 110
Chaplin W. J., Miglio A., 2013, ARA&A, 51, 353
Chaplin W. J., Serenelli A. M., Basu S., Elsworth Y., New R., Verner G. A., 2007, ApJ, 670, 872
Chaplin W. J. et al., 2013, ApJ, 766, 101
Chaplin W. J. et al., 2014, ApJS, 210, 1
Chiappini C., Renda A., Matteucci F., 2002, A&A, 395, 789
Chiosi C., Bertelli G., Bressan A., 1992, ARA&A, 30, 235
Christensen-Dalsgaard J., 2008a, Ap&SS, 316, 13
Christensen-Dalsgaard J., 2008b, Ap&SS, 316, 113
Christensen-Dalsgaard J., 2012, Astron. Nachr., 333, 914
Christensen-Dalsgaard J., Thompson M. J., Gough D. O., 1989, MNRAS, 238, 481
Christensen-Dalsgaard J., Proffitt C. R., Thompson M. J., 1993, ApJ, 403, L75
Christensen-Dalsgaard J., Di Mauro M. P., Houdek G., Pijpers F., 2009, A&A, 494, 205
Christensen-Dalsgaard J. et al., 2010, ApJ, 713, L164
Ciacio F., Degl'innocenti S., Ricci B., 1997, A&AS, 123, 449
Davies G. R., Handberg R., Miglio A., Campante T. L., Chaplin W. J., Elsworth Y., 2014, MNRAS, 445, L94
Davies G. R. et al., 2015, MNRAS, 446, 2959
De Ridder J. et al., 2009, Nature, 459, 398
Deheuvels S., Michel E., 2011, A&A, 535, 91
Demarque P., Guenther D. B., Li L. H., Mazumdar A., Straka C. W., 2008, Ap&SS, 316, 31
Epstein C. R. et al., 2014, ApJ, 785, L28
Fabrycky D. C. et al., 2014, ApJ, 790, 146
Ferguson J. W., Alexander D. R., Allard F., Barman T., Bodnarik J. G., Hauschildt P. H., Heffner-Wong A., Tamanai A., 2005, ApJ, 623, 585
Fogtmann-Schulz A., Hinrup B., Van Eylen V., Christensen-Dalsgaard J., Kjeldsen H., Silva Aguirre V., Tingley B., 2014, ApJ, 781, 67
Formicola A. et al., 2004, Phys. Lett. B, 591, 61
Fressin F. et al., 2011, ApJS, 197, 5
Gai N., Basu S., Chaplin W. J., Elsworth Y., 2011, ApJ, 730, 63
Gilliland R. L. et al., 2013, ApJ, 766, 40
Grec G., Fossat E., Pomerantz M. A., 1983, Sol. Phys., 82, 55
Grevesse N., Sauval A. J., 1998, Space Sci. Rev., 85, 161
Grundahl F., Christensen-Dalsgaard J., Arentoft T., Frandsen S., Kjeldsen H., Jørgensen U. G., Kjaergaard P., 2008, Commun. Asteroseismol., 157, 273

Gruyters P., Korn A. J., Richard O., Grundahl F., Collet R., Mashonkina L. I., Osorio Y., Barklem P. S., 2013, A&A, 555, A31

Gustafsson B., Edvardsson B., Eriksson K., Jørgensen U. G., Nordlund Å., Plez B., 2008, A&A, 486, 951

Guzik J. A., Cox A. N., 1993, ApJ, 411, 394

Howell S. B. et al., 2012, ApJ, 746, 123

Howell S. B. et al., 2014, PASP, 126, 398

Huber D. et al., 2011, ApJ, 743, 143

Huber D. et al., 2012, ApJ, 760, 32

Huber D. et al., 2013a, Science, 342, 331

Huber D. et al., 2013b, ApJ, 767, 127

Huber D. et al., 2014, ApJS, 211, 2

Iglesias C. A., Rogers F. J., 1996, ApJ, 464, 943

Jimenez R., 2003, Science, 299, 1552

Kippenhahn R., Weigert A., Weiss A., 2012, Stellar Structure and Evolution. Springer-Verlag, Berlin

Kjeldsen H., Bedding T. R., 1995, A&A, 293, 87

Kjeldsen H., Bedding T. R., Viskum M., Frandsen S., 1995, AJ, 109, 1313

Kjeldsen H., Bedding T. R., Christensen-Dalsgaard J., 2008, ApJ, 683, L175

Korn A. J., Grundahl F., Richard O., Mashonkina L., Barklem P. S., Collet R., Gustafsson B., Piskunov N., 2007, ApJ, 671, 402

Lebreton Y., Goupil M. J., 2014, A&A, 569, A21

Lin D. N. C., Bodenheimer P., Richardson D. C., 1996, Nature, 380, 606

Lind K., Bergemann M., Asplund M., 2012, MNRAS, 427, 50

Lopez E. D., Fortney J. J., 2013, ApJ, 776, 2

Lund M. N. et al., 2014, A&A, 570, A54

Lundkvist M., Kjeldsen H., Silva Aguirre V., 2014, A&A, 566, 82

Maeder A., 1974a, in Ledoux P., Noels A., Rodgers A. W., eds, Proc. IAU Symp. 59, Stellar Instability and Evolution. Reidel, Dordrecht, p. 109

Maeder A., 1974b, A&A, 32, 177

Maeder A., Meynet G., 1991, A&AS, 89, 451

Magic Z., Serenelli A., Weiss A., Chaboyer B., 2010, ApJ, 718, 1378

Magic Z., Weiss A., Asplund M., 2015, A&A, 573, A89

Marcy G. W. et al., 2014, ApJS, 210, 20

Mathur S. et al., 2012, ApJ, 749, 152

Metcalfe T. S., Charbonneau P., 2003, J. Comput. Phys., 185, 176

Metcalfe T. S., Creevey O. L., Christensen-Dalsgaard J., 2009, ApJ, 699, 373

Metcalfe T. S. et al., 2014, ApJS, 214, 27

Miglio A., 2011, Red Giants as Probes of the Structure and Evolution of the Milky Way. Springer-Verlag Berlin, p. 11

Miglio A., Montalbán J., 2005, A&A, 441, 615

Miglio A. et al., 2012, MNRAS, 419, 2077

Miglio A. et al., 2013a, EPJ Web Conf., 43, 03004

Miglio A. et al., 2013b, MNRAS, 429, 423

Mosser B. et al., 2010, A&A, 517, 22

Nissen P. E., Chen Y. Q., Carigi L., Schuster W. J., Zhao G., 2014, A&A, 568, A25

Norris J. E., 2004, ApJ, 612, L25

North J. R. et al., 2007, MNRAS, 380, L80

Önehag A., Gustafsson B., Korn A., 2014, A&A, 562, A102

Otí Floranes H., Christensen-Dalsgaard J., Thompson M. J., 2005, MNRAS, 356, 671

Pál A. et al., 2008, ApJ, 680, 1450

Perryman M. A. C. et al., 2001, A&A, 369, 339

Pietrinferni A., Cassisi S., Salaris M., Castelli F., 2004, ApJ, 612, 168

Rauer H. et al., 2014, Exp. Astron., 38, 249

Ricker G. R. et al., 2014, Proc. SPIE, 9143, 914320

Rogers F. J., Nayfonov A., 2002, ApJ, 576, 1064

Rogers F. J., Swenson F. J., Iglesias C. A., 1996, ApJ, 456, 902

Rowe J. F. et al., 2014, ApJ, 784, 45

Roxburgh I. W., 2005, A&A, 434, 665

Roxburgh I. W., Vorontsov S. V., 2000, MNRAS, 317, 141

Roxburgh I. W., Vorontsov S. V., 2003, A&A, 411, 215

Roxburgh I. W., Vorontsov S. V., 2013, A&A, 560, A2

Salaris M., Chieffi A., Straniero O., 1993, ApJ, 414, 580

Serenelli A. M., Basu S., 2010, ApJ, 719, 865

Serenelli A. M., Basu S., Ferguson J. W., Asplund M., 2009, ApJ, 705, L123

Serenelli A. M., Bergemann M., Ruchti G., Casagrande L., 2013, MNRAS, 429, 3645

Silva Aguirre V., Ballot J., Serenelli A. M., Weiss A., 2011a, A&A, 529, 63

Silva Aguirre V. et al., 2011b, ApJ, 740, L2

Silva Aguirre V. et al., 2012, ApJ, 757, 99

Silva Aguirre V. et al., 2013, ApJ, 769, 141

Silva Aguirre V. et al., 2014, ApJ, 784, L16

Steffen J. H. et al., 2012, MNRAS, 421, 2342

Steffen J. H. et al., 2013, MNRAS, 428, 1077

Steigman G., 2010, J. Cosmol. Astropart. Phys., 2010, 29

Stello D., Bruntt H., Preston H., Buzasi D., 2008, ApJ, 674, L53

Stello D. et al., 2011, ApJ, 739, 13

Thoul A. A., Bahcall J. N., Loeb A., 1994, ApJ, 421, 828

Trampedach R., Stein R. F., Christensen-Dalsgaard J., Nordlund Å., Asplund M., 2014, MNRAS, 445, 4366

Turcotte S., Richer J., Michaud G., 1998, ApJ, 504, 559

Ulrich R. K., 1986, ApJ, 306, L37

Valle G., Dell'Omodarme M., Prada Moroni P. G., Degl'innocenti S., 2014, A&A, 561, A125

Valle G., Dell'Omodarme M., Prada Moroni P. G., Degl'innocenti S., 2015, A&A, 575, A12

Van Eylen V., Albrecht S., 2015, ApJ, preprint (arXiv:1505.02814)

Van Eylen V. et al., 2014, ApJ, 782, 14

Van Leeuwen F., 2007, A&A, 474, 653

Vandenberg D. A., Gustafsson B., Edvardsson B., Eriksson K., Ferguson J., 2007, ApJ, 666, L105

Weiss A., Schlattl H., 2008, Ap&SS, 316, 99

White T. R., Bedding T. R., Stello D., Christensen-Dalsgaard J., Huber D., Kjeldsen H., 2011, ApJ, 743, 161

White T. R. et al., 2013, MNRAS, 433, 1262

Woitaszek M., Metcalfe T., Shorrock I., 2009, in Proc. 5th Grid Computing Environments Workshop (GCE 2009), AMP: A Science-Driven Web-Based Application for the TeraGrid. ACM, New York, p. 1

Xie J.-W., 2014, ApJS, 210, 25

SUPPORTING INFORMATION

Additional Supporting Information may be found in the online version of this paper:

Table 3. The full table is available in electronic format on the journal website.
Table A1. Stellar properties determined with ASTFIT.
Table A2. Stellar properties determined with YMCM.
Table A3. Stellar properties determined with AMP.
(http://mnras.oxfordjournals.org/lookup/suppl/doi:10.1093/mnras/stv1388/-/DC1).

Please note: Oxford University Press are not responsible for the content or functionality of any supporting materials supplied by the authors. Any queries (other than missing material) should be directed to the corresponding author for the paper.

APPENDIX A: EVOLUTIONARY CODES AND FITTING ALGORITHMS

In the following sections, we describe the fitting procedures used to determine stellar properties for our sample, including the evolutionary and pulsation codes used.

A1 ASTFIT

The ASTFIT method uses the Aarhus stellar evolution (ASTEC; Christensen-Dalsgaard 2008a) and pulsation (ADIPLS; Christensen-Dalsgaard 2008b) codes. It is based on fitting individual model frequencies, applying a correction for the surface errors, to the

observed frequencies (see also Gilliland et al. 2013). The fit is carried out in grid of models varying the mass and composition. The chemical composition is based on a helium enrichment relation $\Delta Y/\Delta Z = 1.4$, set up in terms of initial hydrogen and heavy-element abundances (X_0, Z_0), with three neighbouring values of Z_0 for each value of X_0. The grid extends in [Fe/H] between -0.577 and 0.415 in steps of around 0.05 and in mass between 0.7 and 1.69 $M_\odot$, in steps of 0.01 $M_\odot$. The ASTFIT results presented here were computed without diffusion and settling, and convective core overshoot was not considered. The mixing-length parameter was set to $\alpha_{MLT} = 1.8$, roughly corresponding to solar calibration. The model physics otherwise essentially followed the BASTA specifications.

The fit of a given model to the data is defined in terms of

$$\chi_\nu^2 = \frac{1}{N-1} \sum_{i=1}^{N} \left(\frac{\nu_i^{(\mathrm{obs})} - \nu_i^{(\mathrm{mod})}}{\sigma_i} \right)^2 , \tag{A1}$$

where $\nu_i^{(\mathrm{obs})}$ and $\nu_i^{(\mathrm{mod})}$ are the observed and model frequencies and σ_i is the error in the observed frequencies. Here the model frequencies typically include a surface correction (see Section A1.1 below). It is assumed that the degree and order of the observed frequencies have already been determined, and that they do not include additional mixed modes. Hence, when the models contain mixed modes, they are excluded (renumbering the remaining modes) retaining only the most acoustically dominated modes (as determined from their inertia) in each interval in large frequency separation $\Delta\nu$. The fit also includes

$$\chi_{\mathrm{spec}}^2 = \left(\frac{T_{\mathrm{eff}}^{(\mathrm{obs})} - T_{\mathrm{eff}}^{(\mathrm{mod})}}{\sigma(T_{\mathrm{eff}})} \right)^2 + \left(\frac{[\mathrm{Fe/H}]^{(\mathrm{obs})} - [\mathrm{Fe/H}]^{(\mathrm{mod})}}{\sigma([\mathrm{Fe/H}])} \right)^2 \tag{A2}$$

with the observed and model effective temperature T_{eff} and [Fe/H]. The complete fit is then characterized by $\chi^2 = \chi_\nu^2 + \chi_{\mathrm{spec}}^2$, defining the relative weight between the oscillation and the spectroscopic data.

For each evolution sequence, frequencies are calculated for at least every second timestep. Amongst these frequency sets, the model $\mathcal{M}'_{\mathrm{min}}$ with the smallest χ_ν^2 is determined. Based on homology scaling, it is assumed that the frequencies in the vicinity of $\mathcal{M}'_{\mathrm{min}}$ can be obtained as $r\nu_i(\mathcal{M}'_{\mathrm{min}})$, where $r = [R/R(\mathcal{M}'_{\mathrm{min}})]^{-3/2}$, R being the surface radius of the model, and the best-fitting model is determined by minimizing

$$\chi_\nu^2(r) = \frac{1}{N-1} \sum_{i=1}^{N} \left(\frac{\nu_i^{(\mathrm{obs})} - r\nu_i(\mathcal{M}'_{\mathrm{min}})}{\sigma_i} \right)^2 \tag{A3}$$

as a function of r. The resulting value r_{min} of r defines an estimate R_{min} of the radius of the best-fitting model along the given sequence.

The other properties of this best-fitting model, for the given set of model parameters $\{\mathcal{P}_k\}$ and with corresponding $\chi_{\nu,\mathrm{min}}^2(\mathcal{P}_k)$, are determined by linear interpolation in R to R_{min}. The corresponding minimum $\chi_{\mathrm{min}}^2(\mathcal{P}_k)$ is then determined as $\chi_{\mathrm{min}}^2(\mathcal{P}_k) = \chi_{\nu,\mathrm{min}}^2(\mathcal{P}_k) + \chi_{\mathrm{spec}}(\mathcal{M}'_{\mathrm{min}})$.[3] The final best-fitting model is found as the parameter set corresponding to the smallest $\chi_{\nu,\mathrm{min}}^2(\mathcal{P}_k)$ (or $\chi_{\mathrm{min}}^2(\mathcal{P}_k)$) over a suitable selection of models in the grid.

It is very informative to plot $\chi_{\nu,\mathrm{min}}^2(\mathcal{P}_k)$ or $\chi_{\mathrm{min}}^2(\mathcal{P}_k)$ against the various model properties, such as mean density $\langle\rho\rangle$, R, or age. Representative results are given in the HAT-P-7 paper (Christensen-

---

[3] and hence neglecting the generally negligible change in, e.g., T_{eff} between timesteps.

Dalsgaard et al. 2010). The best-fitting frequencies, e.g. for comparison with the observations in an échelle diagram, are obtained by applying the appropriate scaling r_{min} to the frequencies of the model $\mathcal{M}'_{\mathrm{min}}$ in the minimizing sequence.

Although probably not completely justified in a statistical sense, estimates of stellar properties, in particular radius, mass, and age, are determined as averages and standard deviations of the properties of the models $\mathcal{M}_{\mathrm{min}}(\mathcal{P}_k)$ over the parameters $\{\mathcal{P}_k\}$, with the weights $\exp(-\chi_{\mathrm{min}}^2(\mathcal{P}_k)/2)$, corresponding to the likelihood. These are the final ASTFIT results compared with the BASTA results in Figs 10 and 11 and presented in Table A1.

A1.1 Near-surface correction

It is well established that errors in the modelling of the structure of the near-surface layers of the star and their effects on the oscillations cause systematic differences between the model and observed frequencies, even when the model otherwise matches the structure of the star. This is particularly evident in the solar case, where the availability of frequencies over a broad range of degrees allows separation between the effects of the bulk of the solar interior and the surface layers. These errors must be taken into account when, as done in ASTFIT, individual model frequencies are fitted to the observations. The correction unavoidably requires prior and perhaps poorly justified assumptions, typically based on the behaviour determined in the solar case.

Here we specifically use a representation of the surface correction that has a functional form matching the solar behaviour (see also Aerts, Christensen-Dalsgaard & Kurtz 2010; Christensen-Dalsgaard 2012). This is obtained from the differential form of the Duvall asymptotic expression for the frequencies (Christensen-Dalsgaard, Thompson & Gough 1989), according to which the frequency differences $\delta\nu$ between the Sun and a model satisfy

$$S_{nl} \frac{\delta\nu_{nl}}{\nu_{nl}} \simeq \mathcal{H}_1(\nu_{nl}/L) + \mathcal{H}_2(\nu_{nl}) , \tag{A4}$$

where $L = \sqrt{l(l+1)}$ and S_{nl} is a scale factor which can be calculated from the model, and which may be chosen to be close to 1 for low-degree modes. The term in $\mathcal{H}_1$ reflects the difference in sound speed between the Sun and the model throughout the star, whereas $\mathcal{H}_2$ contains the contribution from the near-surface region. Since on general grounds the surface effects are very small at low frequency, the arbitrary additive constant in the definition of $\mathcal{H}_2$ may be chosen such that $\mathcal{H}_2$ is zero at low frequency. In Fig. A1 is shown the frequency shift $\delta\nu_\odot^{(\mathrm{surf})}$ caused by the surface effects in the Sun, determined in this manner from $\nu\mathcal{H}_2(\nu)$. We now make the assumption that the correction in other stars has a similar functional form, in terms of frequency measured in units the acoustic cut-off frequency ν_{ac}, which provides a physically motivated frequency scale for the stellar atmosphere. Thus, for each set of model frequencies, we obtain the surface correction by determining a scale factor r and an amplitude $\tilde{a}$ from a least-squares fit of

$$\nu_{nl} = r\nu_{nl}^{(\mathrm{ref})} + \tilde{a}\mathcal{G}_\odot(\nu_{nl}/\nu_{\mathrm{ac}}) \tag{A5}$$

to the observed frequencies, where the function $\mathcal{G}_\odot$ is determined from $\nu\mathcal{H}_2(\nu)$, illustrated in Fig. A1, using a solar acoustic cut-off frequency of $\nu_{\mathrm{ac},\odot} = 5200 \,\mu\mathrm{Hz}$. The model frequencies in equation (A1) are obtained from this expression, but without including the scale factor.

Table A1. Stellar properties determined with ASTFIT. Solar luminosity used $L_\odot = 3.846 \times 10^{33}$ (erg s^{-1}). The first five objects are shown here for guidance on the format, and the full table is available online.

| KOI	KIC	Mass ($M_\odot$)	Radius ($R_\odot$)	Density (g cm^{-3})	log g (dex)	Luminosity ($L_\odot$)	Age (Gyr)
2	10666592	1.538 ± 0.030	2.000 ± 0.012	0.271 ± 0.002	4.023 ± 0.004	5.811 ± 0.213	1.88 ± 0.14
5	8554498	1.173 ± 0.020	1.785 ± 0.010	0.291 ± 0.001	4.004 ± 0.003	3.373 ± 0.133	6.12 ± 0.28
7	11853905	1.118 ± 0.031	1.553 ± 0.013	0.420 ± 0.002	4.104 ± 0.005	2.488 ± 0.117	7.27 ± 0.69
41	6521045	1.121 ± 0.012	1.517 ± 0.006	0.452 ± 0.001	4.125 ± 0.002	2.509 ± 0.088	6.83 ± 0.28
42	8866102	1.218 ± 0.036	1.354 ± 0.013	0.691 ± 0.004	4.260 ± 0.005	2.654 ± 0.111	2.78 ± 0.47
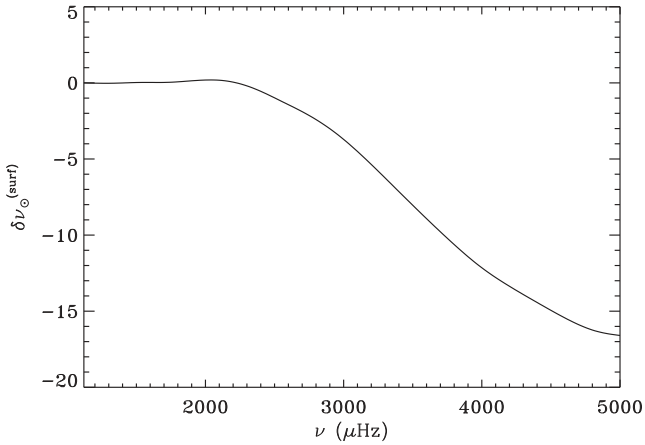
Figure A1. The solar surface correction $\delta_\odot^{(\mathrm{surf})}$ determined from $\mathcal{H}_2$ in the fit given in equation (A4) to solar data over a broad range of degrees.

A2 YMCM

The YMCM used the YREC (Demarque et al. 2008) code to model the stars. While the input physics was the same as in the other techniques, the method of constructing the models was very different.

The starting point of the modelling effort for each star was the average large separation that was used in the grid-based modelling, the mass obtained from grid-based modelling, and the effective temperature and metallicity obtained from spectroscopy. Since each of these quantities is associated with an uncertainty, we created many more realizations of these parameters to obtain a larger set of $(M, \Delta\nu, T_{\mathrm{eff}}, [\mathrm{Fe/H}])$. The $\Delta\nu$ in each set, along with M, was used to calculate R using the usual scaling relationship. Since the scaling relationship is not exact, we used the empirical correction of White et al. (2011) to get a better estimate.

For each combination $(M, R, T_{\mathrm{eff}}, [\mathrm{Fe/H}])$, we used YREC in an iterative mode to obtain a model of the given mass M and [Fe/H] than had the required R and T_{eff}. Since the mixing-length parameter was set to be the solar-calibrated value (1.6756 for the given physics and formulation of mixing-length theory in YREC), the only free parameter we had was the initial helium abundance Y_0 that was varied until the required model was obtained. Some combinations of parameters resulted in models that need Y_0 to be lower than the primordial helium abundance; all such models were rejected.

Theoretical frequencies of oscillation are computed using the code first described by Antia & Basu (1994). The χ^2 for the differences between the observed frequencies and those of the models, χ_ν^2, were calculated after correcting for the surface term in a manner outlined below. Similarly, we calculated χ_{rat}^2 for the differences in the frequency ratios r_{010} and r_{02} (including correlations), $\chi_{T_{\mathrm{eff}}}^2$ for

the difference in effective temperature, and $\chi_{[\mathrm{Fe/H}]}^2$ for the difference in metallicity. The final goodness of fit was determined by

$$\chi_{\mathrm{tot}}^2 = \chi_\nu^2 + \chi_{\mathrm{rat}}^2 + \chi_{T_{\mathrm{eff}}}^2 + \chi_{[\mathrm{Fe/H}]}^2. \tag{A6}$$

The best-fitting model was the one with the lowest value of χ_{tot}^2.

We used the scaled solar surface term to correct the frequency differences between the observed and model frequencies. We first constructed a solar model with the same physics as the rest of the models and determined its frequency differences with respect to observed solar frequencies obtained by the Birmingham Solar Oscillations Network (BiSON) and listed in table 1 of Chaplin et al. (2007). The solar surface term was obtained by fitting these frequency differences to the differential form of the Duvall law (Christensen-Dalsgaard et al. 1989). We denote this as the $\nu_{nl,\odot}-\delta\nu_{nl,\odot}$ relation. Both $\nu_{nl,\odot}$ and $\delta\nu_{nl,\odot}$ are then scaled to the mass and radius of the stellar model under consideration using the homology scaling

$$r = \frac{\langle\Delta\nu(\mathrm{mod})\rangle}{\langle\Delta\nu_\odot\rangle}, \tag{A7}$$

where the angular brackets denote the average. The resulting $r\nu_{nl,\odot}-r\delta\nu_{nl,\odot}$ is then used to correct the stellar model for the surface term. The corrected frequencies are denoted as

$$\nu_{nl}^{(\mathrm{corr})} = \nu_{nl}^{(\mathrm{mod})} + \beta r\delta\nu_{nl,\odot}, \tag{A8}$$

with $r\delta\nu_{nl,\odot}$ evaluated at $r\nu_{nl,\odot}=\nu_{nl}(\mathrm{obs})$. The factor β is selected to minimize

$$\sum \frac{\left(\nu_{nl}^{(\mathrm{obs})} - \nu_{nl}^{(\mathrm{corr})}\right)^2}{\sigma^2(\nu_{nl})}. \tag{A9}$$

$\nu_{nl}^{(\mathrm{corr})}$ are then used to calculate χ_ν^2. The final set of stellar properties determined with the YMCM are available in Table A2.

A3 AMP

For the results presented in Section 4.3, we used the AMP (Metcalfe, Creevey & Christensen-Dalsgaard 2009; Woitaszek, Metcalfe & Shorrock 2009) in a similar configuration as that described in Metcalfe et al. (2014), but without including diffusion and settling of helium. In summary, AMP uses a parallel genetic algorithm (GA; Metcalfe & Charbonneau 2003) to optimize the match between stellar model output and the available set of observational constraints. The evolution models are produced with ASTEC, and the oscillation frequencies are calculated with ADIPLS. The five adjustable model parameters include the mass (M), age (t), composition (Z and Y_i), and mixing length (α). The oscillation frequencies and other properties of each model are compared to four sets of observational constraints, including (1) the individual

Table A2. Stellar properties determined with YMCM. Solar luminosity used $L_\odot = 3.846 \times 10^{33}$ (erg s^{-1}). The first five objects are shown here for guidance on the format, and the full table is available online.

KOI	KIC	Mass (M$_\odot$)	Radius (R$_\odot$)	Density (g cm^{-3})	log g (dex)	Luminosity (L$_\odot$)	Age (Gyr)	$Y_{\rm ini}$	$Z_{\rm ini}$
2	10666592	1.546 ± 0.035	2.001 ± 0.016	0.272 ± 0.002	4.024 ± 0.004	5.744 ± 0.175	1.63 ± 0.10	0.278 ± 0.017	0.0282 ± 0.0038
7	11853905	1.146 ± 0.030	1.567 ± 0.014	0.419 ± 0.005	4.107 ± 0.005	2.533 ± 0.100	6.93 ± 0.55	0.257 ± 0.013	0.0232 ± 0.0026
41	6521045	1.138 ± 0.009	1.525 ± 0.004	0.452 ± 0.001	4.127 ± 0.001	2.564 ± 0.048	6.22 ± 0.14	0.267 ± 0.006	0.0219 ± 0.0020
42	8866102	1.238 ± 0.041	1.359 ± 0.015	0.694 ± 0.003	4.264 ± 0.005	2.671 ± 0.083	2.32 ± 0.31	0.268 ± 0.016	0.0187 ± 0.0021
69	3544595	0.919 ± 0.020	0.922 ± 0.007	1.650 ± 0.002	4.471 ± 0.003	0.771 ± 0.028	7.04 ± 0.68	0.252 ± 0.015	0.0133 ± 0.0015

Table A3. Stellar properties determined with AMP. Solar luminosity used $L_\odot = 3.846 \times 10^{33}$ (erg s^{-1}). The first five objects are shown here for guidance on the format, and the full table is available online.

KOI	KIC	Mass (M$_\odot$)	Radius (R$_\odot$)	Density (g cm^{-3})	log g (dex)	Luminosity (L$_\odot$)	Age (Gyr)	$Y_{\rm ini}$	$Z_{\rm ini}$	$\alpha_{\rm MLT}$
2	10666592	1.300 ± 0.055	1.879 ± 0.018	0.276 ± 0.001	4.004 ± 0.003	5.096 ± 0.291	2.79 ± 0.52	0.317 ± 0.011	0.0239 ± 0.0043	1.72 ± 0.13
5	8554498	1.310 ± 0.038	1.825 ± 0.018	0.303 ± 0.001	4.032 ± 0.005	3.444 ± 0.190	4.56 ± 0.60	0.243 ± 0.011	0.0255 ± 0.0032	1.44 ± 0.09
7	11853905	1.140 ± 0.017	1.553 ± 0.016	0.428 ± 0.008	4.112 ± 0.007	2.435 ± 0.185	6.13 ± 0.30	0.268 ± 0.012	0.0217 ± 0.0027	1.62 ± 0.12
41	6521045	1.090 ± 0.018	1.501 ± 0.013	0.454 ± 0.008	4.123 ± 0.005	2.337 ± 0.129	7.16 ± 0.42	0.265 ± 0.010	0.0184 ± 0.0012	1.78 ± 0.07
42	8866102	1.260 ± 0.032	1.363 ± 0.014	0.701 ± 0.004	4.269 ± 0.003	2.626 ± 0.137	2.01 ± 0.47	0.257 ± 0.012	0.0184 ± 0.0015	1.82 ± 0.09

frequencies corrected for surface effects following the empirical prescription of Kjeldsen et al. (2008), (2) the frequency ratios r_{02} defined by equation (2), (3) the frequency ratios r_{010} defined by equation (6), and (4) the available spectroscopic constraints. A normalized χ^2 is calculated for each set of constraints, and the GA attempts to minimize the mean of the four χ^2 values. This allows the various asteroseismic quality metrics to be traded off against each other, while ensuring that the numerous frequencies and ratios do not overwhelm the relatively few spectroscopic constraints. The interested reader can find the optimal model parameters produced by AMP for each star in Table A3.

[1] *Stellar Astrophysics Centre, Department of Physics and Astronomy, Aarhus University, Ny Munkegade 120, DK-8000 Aarhus C, Denmark*

[2] *School of Physics and Astronomy, University of Birmingham, Birmingham B15 2TT, UK*

[3] *Department of Astronomy, Yale University, PO Box 208101, New Haven, CT 06520-8101, USA*

[4] *Institut d'Astrophysique Spatiale, CNRS, UMR 8617, Université Paris XI, Batiment 121, F-91405 Orsay Cedex*

[5] *Laboratoire Lagrange, Université Côte d'Azur, Observatoire de la Côte d'Azur, CNRS, Blvd de l'Observatoire, CS 34229, F-06304 Nice cedex 4, France*

[6] *Space Science Institute, 4750 Walnut St. Suite 205, Boulder, CO 80301, USA*

[7] *Sydney Institute for Astronomy (SIfA), School of Physics, University of Sydney, NSW 2006, Australia*

[8] *Research School of Astronomy & Astrophysics, Mount Stromlo Observatory, The Australian National University, ACT 2611, Australia*

[9] *SETI Institute, 189 Bernardo Avenue, Mountain View, CA 94043, USA*

[10] *Instituto de Ciencias del Espacio (ICE-CSIC/IEEC), Campus UAB, Carrer de Can Magrans s/n, E-08193 Cerdanyola del Valles, Barcelona, Spain*

[11] *Center for Exoplanets and Habitable Worlds, The Pennsylvania State University, University Park, PA 16802, USA*

[12] *Max-Planck-Institut für Sonnensystemforschung, Justus-von-Liebig-Weg 3, D-37077 Göttingen, Germany*

[13] *Department of Geoscience, Aarhus University, Høegh-Guldbergs Gade 2, DK-8000 Aarhus C, Denmark*

[14] *Department of Physics and Astronomy, Iowa State University, Ames, IA 50014, USA*

This paper has been typeset from a TeX/LaTeX file prepared by the author.